Direct numerical simulations of homogeneous turbulence subject to periodic shear

By DAZHI YU AND SHARATH S. GIRIMAJI

Department of Aerospace Engineering, Texas A&M University, College Station, TX 77843-3141, USA

We perform direct numerical simulations (DNS) of homogeneous turbulence subject to periodic shear – $S = S_{max} \sin(\omega t)$, where ω is the forcing frequency and S_{max} is the maximum shear. The lattice Boltzmann method (LBM) is employed in our simulations and a periodic body force is introduced to produce the required shear. We find that the turbulence behaviour is a strong function of the forcing frequency. There exists a critical frequency – $\omega_{cr}/S_{max} \approx 0.5$ – at which the observed behaviour bifurcates. At lower forcing frequencies ($\omega < \omega_{cr}$), turbulence is sustained and the kinetic energy grows. At higher frequencies, the kinetic energy decays. It is shown that the phase difference between the applied strain and the Reynolds stress decreases monotonically from π in the constant shear case to $\pi/2$ in very high frequency shear cases. As a result, the net turbulence production per cycle decreases with increasing frequency. In fact, at $\omega/S_{max} \geqslant 10$, decaying isotropic turbulence results are recovered. The frequency-dependence of anisotropy and Reynolds stress budget are also investigated in detail. It is shown that inviscid rapid distortion theory (RDT) does not capture the observed features: it predicts purely oscillatory behaviour at all forcing frequencies. Second moment closure models do predict growth at low frequencies and decay at high frequencies, but the critical frequency value is underestimated. The challenges posed by this flow to turbulence closure modelling are identified.

1. Introduction

Over the last two decades, much progress has been made in understanding and predicting turbulent flows. During this period, direct numerical simulations (DNS) have played a crucial role, especially in providing insight into fundamental turbulence processes (Moin & Mahesh 1998). However, much of this progress is restricted to turbulent flows subject to steady forcing. There are numerous turbulent flows in engineering and nature in which turbulence is subject to time-dependent (unsteady) forcing, e.g. flows in turbines, internal combustion engines, and biological devices. An important feature of unsteadily forced flows is the emergence of phase difference between mean strain (rate) and Reynolds stress, which leads to significant changes in the turbulence dynamics from the constant forcing case. There are many flow control strategies attempting to take advantage of unsteady turbulence dynamics to modify or control flows (Quadrid & Sibilla 2000).

Detailed investigations of turbulence subject to unsteady forcing are relatively recent. Unsteady forcing implies a time-varying mean-velocity gradient which encompasses a very wide range of possibilities. Presumably, different types of unsteadiness can have vastly different effects on turbulence. This renders a systematic study of unsteadily forced turbulence difficult. However, some progress can be made by

recognizing that any arbitrary unsteadiness in the mean velocity gradient can be expressed as a combination of four elementary forms of variation: (i) temporal changes in the eigenvalues of the mean strain rate tensor, with eigen-directions fixed; (ii) rotation of the eigen-directions of the mean strain rate tensor, with eigenvalues maintained constant; (iii) temporal changes of the mean vorticity-vector magnitude, with the direction fixed; and, (iv) rotation of the mean vorticity-vector axis, with its magnitude maintained constant. Our ultimate goal is to study, in isolation, the effects of each type of unsteadiness on turbulence.

To accumulate a reliable knowledge base of these flows, we must revisit many of the canonical flows and re-examine the turbulence features in the context of unsteady forcing. An idealized flow which has contributed greatly to our current understanding of steadily forced turbulence is the homogeneous shear flow. Examination of the unsteady counterparts of this important flow will provide valuable insight into the physics of many different practical turbulent flows. Two forms of unsteady homogeneous shear flow are currently under investigation in our group. The first is a homogeneous periodic shear flow which is the subject of this paper. The mean velocity gradient of this flow is given by

$$\frac{\partial U_i}{\partial x_j}(t) = S_{max} \sin(\omega t)\delta_{i1}\delta_{j2}. \tag{1.1}$$

Here, and throughout the paper, we use the following notation: $\boldsymbol{V}$, $\boldsymbol{U}$ and $\boldsymbol{u}$ represent the total, mean and fluctuating velocity vectors. Thus, the mean-strain tensor has fixed eigen-directions and temporally sinusoidal eigenvalues (elementary form (i) in the above list). In our DNS (direct numerical simulation) investigation, the desired velocity gradient is produced by introducing a body force which is a deterministic function of space and time. This issue will be discussed in detail later. The second form of unsteady homogeneous shear which is being investigated in a concurrent study is a rotating shear flow. In this flow, the eigenvalues of the mean strain-rate tensor are constant, but the eigen-directions rotate at a constant rate (elementary form (ii)). When the rotation rate is zero, the forcing reduces to a simple homogeneous shear. Again, the required time-varying velocity field is produced using a body force. The results of turbulence subject to rotating shear is reported in Girimaji, O'Neil & Yu (2006).

1.1. *Relevant literature*

Some of the classical experiments of steady homogeneous shear flow include the works of Rose (1966), Champagne, Harris & Corrsin (1970), Tavoularis & Corrsin (1981*a*, *b*), and De Souza, Nguyen & Tavoularis (1995). Tavoularis & Karnik (1989) claim that such flow exhibits an asymptotic self-preserving structure, in which the dimensionless Reynolds stress ratio and the production-to-dissipation ratio remain essentially constant. At that asymptotic stage, the measured values of the anisotropy tensor components b_{ij} are: $b_{11} = 0.18 \pm 0.04$, $b_{22} = -0.11 \pm 0.02$ and $b_{12} = -0.16 \pm 0.01$. The anisotropy tensor is defined as $b_{ij} = \langle u_i u_j \rangle / 2k - \delta_{ij}/3$. The applied mean shear, turbulent kinetic energy, production and dissipation are represented by $S = \mathrm{d}U/\mathrm{d}y$, k, P and ε, respectively. Normalized shear is given by $S^* = Sk/\varepsilon$. The measured asymptotic production-to-dissipation ratio P/ε is 1.47 ± 0.06 and normalized shear is $S^* = 5.6$. All these findings have directly contributed toward turbulence closure modelling (Girimaji 2000, and works listed therein). For example, the asymptotic anisotropy values are used in the calibration of the various coefficients in rapid pressure–strain closure models. The asymptotic production-to-dissipation ratio is directly related to a coefficient in the modelled dissipation evolution equation.

Direct numerical simulations have been performed to study aspects of steady homogeneous shear flows not easily accessible to experimental investigation. Rogers & Moin (1987) examined the structure of vorticity in homogeneous turbulent shear flows. Lee, Kim & Moin (1990) compared the structure of turbulence subject to high shear rate in homogeneous shear flow with that in turbulent channel flow, and found that many dynamical features in the two flows are similar. Kida & Tanaka (1994) investigated the regeneration cycle of the streamwise vortices in a homogeneous shear flow. The small-scale structure of homogeneous shear flow has been found to share many common features with those of other strain-dominated turbulent flows. Based on the above observations, we suggest that the investigation of unsteadily forced turbulence should start with homogeneous shear flows.

Rotating homogeneous shear flow shares some common features with the homogeneous turbulence subject to periodic shear (elementary form (i)) and rotating shear (elementary form (ii)). When considered in the inertial frame, it is clear that the eigen-directions of the applied shear rotate, and turbulence is subjected to time-dependent forcing. Rotating homogeneous shear flow has been the subject of many theoretical and computational studies (Speziale, Gatski & Giolla Mhuiris 1990; Speziale, Abid & Blaisdell 1996; Sahli & Cambon 1997; Sahli, Cambon & Speziale 1997; Sahli 2002). The major findings from these studies are: (*a*) for small rates of rotation (Ω) relative to shear S, turbulence grows in time, although slower than in the non-rotating shear case; and, (*b*) for high rates of rotation, fluctuations become two-dimensional (as per the Taylor–Proudman theorem) and turbulence decays. It is found that the observed behaviour is well predicted by linear stability theory. Linear stability equations predict that turbulence can be sustained only for the range of parameter values $0 \leqslant |\Omega|/S \leqslant 0.5$. This range is very close to that observed in experiments and second-moment closure model calculations.

Another interesting unsteady flow in which turbulence is subject to successive mean compression and dilatation was investigated by Hadzic, Hanjalic & Laurence (2001). It was found that a phase lag between Reynolds stress and mean strain developed shortly after introduction of periodic forcing. At all forcing frequencies, turbulence was found to decay at long times.

1.2. *Objective and methodology*

In this paper, our objective is to perform DNS of homogeneous flows subject to periodic (sinusoidal) mean shear. The goal is to gain important insight into various physical processes and evaluate the applicability of current turbulent closures. While most DNS studies in the past have employed the Navier–Stokes equations (NS-DNS), we will use the lattice Boltzmann method in our work (LBM-DNS).

The lattice Boltzmann method (LBM) is emerging as a promising alternative for computing fluid dynamics problems (Succi 2001; Yu *et al.* 2003). Historically, the LBM was developed from lattice gas automata (McNamara & Zanetti 1988). The theoretical foundation of the LBM was established by McNamara & Zanetti (1988), Higuera & Jimenez (1989), Koelman (1991), Chen, Chen & Matthaeus (1992), d'Humières (1992) and Qian, d'Humières & Lallemand (1992). The LBM has been used mostly to simulate different kinds of low-Reynolds-number flows. Direct numerical simulation of turbulence using LBM is more recent. In previous works, we have established the physical accuracy and computational advantages of using LBM-DNS and LBM-LES in decaying isotropic turbulence in inertial and rotating frames (Yu, Girimaji & Luo 2005*a*, *b*). In Yu & Girimaji (2005), we demonstrate the capability of LBM-DNS in steady homogeneous shear flow as well. At this stage, LBM is well validated for

DNS of steadily forced turbulent flows. In this paper, we extend the LBM algorithm developed in Yu & Girimaji (2005) to periodic homogeneous shear turbulent flow by introducing an appropriate body force.

We address the following issues as a function of forcing frequency:

(*a*) Evolution of turbulence statistics such as kinetic energy, production, dissipation and Reynolds stress anisotropy;

(*b*) Phase lag between applied mean strain and Reynolds stress;

(*c*) Budgets of Reynolds stress;

(*d*) Comparison of DNS results with rapid distortion theory (RDT) and second moment closure models.

The reminder of this paper is organized as follows. A brief introduction to the lattice Boltzmann method is given in §2. In §3, we develop the methodology for generating homogeneous turbulence field subject to time-dependent mean velocity gradients. We present the DNS fluctuating velocity equations along with RDT and RANS closure equations. Computational issues including the validation of the LBM procedure used here are discussed in §4. In §5, the results of LBM-DNS of homogeneous turbulence subjected to periodic shear are presented and the new physical features are identified. In §6, we compare the DNS results with predictions from RDT and two second-moment closure Reynolds-averaged Navier–Stokes (RANS) turbulence models. Finally, we conclude with summary and discussion in §7.

2. Lattice Boltzmann equation

As the use of lattice Boltzmann method for turbulence computations is still somewhat novel, we will provide a brief introduction. The reader is directed to the references provided for detailed treatment of the various LBM issues.

The Boltzmann equation deals with the single particle distribution function $f(\boldsymbol{x}, \boldsymbol{\xi}, t)$, where $\boldsymbol{\xi}$ is the particle velocity, in phase space $(\boldsymbol{x}, \boldsymbol{\xi})$ at time t. One popular kinetic model is the Boltzmann equation simplified with Bhatnagar–Gross–Krook (BGK) approximation (Bhatnagar, Gross & Krook 1954):

$$\frac{\partial f}{\partial t} + \boldsymbol{\xi} \cdot \nabla f = -\frac{1}{\lambda} \big[f - f^{(0)} \big], \qquad (2.1)$$

where $f^{(0)}$ is the equilibrium distribution function (the Maxwell–Boltzmann distribution function), and λ is the relaxation time. The mass density ρ and momentum density $\rho \boldsymbol{V}$ are the first $(D+1)$ hydrodynamic moments of the distribution function f and $f^{(0)}$, where D is the dimension of velocity space.

To solve f numerically, (2.1) can be discretized in the velocity space $\boldsymbol{\xi}$ using a finite set of velocities $\{\boldsymbol{\xi}_\alpha\}$ without affecting the conserved hydrodynamic moments (He & Luo 1997),

$$\frac{\partial f_\alpha}{\partial t} + \boldsymbol{\xi}_\alpha \cdot \nabla f_\alpha = -\frac{1}{\lambda} \big[f_\alpha - f_\alpha^{(eq)} \big]. \qquad (2.2)$$

In (2.2), $f_\alpha(\boldsymbol{x}, t) \equiv f(\boldsymbol{x}, \boldsymbol{\xi}_\alpha, t)$ and $f_\alpha^{(eq)} = f^{(0)}(\boldsymbol{x}, \boldsymbol{\xi}_\alpha, t)$ are, respectively, the current distribution function and the equilibrium distribution function of the αth discrete velocity $\boldsymbol{\xi}_\alpha$. Thus the LBM belongs in the class of discrete velocity methods (DVM) for flow description.

In the LBM, physical space is discretized coherently with particle velocity space to preserve the conservation laws and ensure the correct behaviour of macroscopic variables. The lattice Boltzmann equation with the Bhatnagar–Gross–Krook (BGK)

approximation is

$$f_\alpha(\boldsymbol{x}_i + \boldsymbol{e}_\alpha \delta t, t + \delta t) - f_\alpha(\boldsymbol{x}_i, t) = -\frac{1}{\tau}\left[f_\alpha(\boldsymbol{x}_i, t) - f_\alpha^{(eq)}(\boldsymbol{x}_i, t)\right], \tag{2.3}$$

where $\tau = \lambda/\delta t$ and δx and δt are the lattice constants and the time step, respectively. With the velocity space discretized, the hydrodynamic moments of f and $f^{(eq)}$ are evaluated from the following quadrature formulae:

$$\rho = \sum_\alpha f_\alpha = \sum_\alpha f_\alpha^{(eq)}, \tag{2.4}$$

$$\rho \boldsymbol{V} = \sum_\alpha \boldsymbol{e}_\alpha f_\alpha = \sum_\alpha \boldsymbol{e}_\alpha f_\alpha^{(eq)}. \tag{2.5}$$

Many choices of lattice model are available in literature. The 9-velocity (or 9-bit) model on the two-dimensional square lattice, denoted as the D2Q9 model, has been widely used for simulating two-dimensional flows. For three-dimensional flows, several cubic lattice models, such as the 15-bit (D3Q15), 19-bit (D3Q19) and 27-bit (D3Q27) models are available. For athermal fluids, the equilibrium distributions of the D2Q9, D3Q15, D3Q19 and D3Q27 models are all of the form (Qian *et al.* 1992):

$$f_\alpha^{(eq)} = \rho w_\alpha \left[1 + \frac{3}{c^2}\boldsymbol{e}_\alpha \cdot \boldsymbol{V} + \frac{9}{2c^4}(\boldsymbol{e}_\alpha \cdot \boldsymbol{V})^2 - \frac{3}{2c^2}\boldsymbol{V}\cdot \boldsymbol{V}\right], \tag{2.6}$$

where w_α is a weighting factor and $\boldsymbol{e}_\alpha$ is a discrete velocity, $c = \delta x/\delta t$ is the lattice speed. It can be shown that $f_\alpha^{(eq)}$ is in fact a finite-term Taylor series expansion of the Maxwellian $f^{(0)}$. This approximation of $f^{(0)}$ by the above $f_\alpha^{(eq)}$ makes the method valid only in the incompressible limit ($|\boldsymbol{V}|/c \to 0$). In the above models, the speed of sound is $c_s = c/\sqrt{3}$ and the equation of state is that of an ideal gas $p = \rho c_s^2$. The viscosity of the fluid is

$$\nu = (\tau - 0.5)c_s^2 \delta t. \tag{2.7}$$

It should be noted that (2.3) is explicit, easy to implement, and straightforward to parallelize. In this paper, we choose the 19-bit (D3Q19) model because of its advantages in matters of stability and efficiency (Mei *et al.* 2000). The macroscopic (continuum) mass and momentum balance dictated by this lattice Boltzmann equation are exactly the same as those of Navier–Stokes equations in the incompressible limit. In fact, in discussing the LBM macroscopic characteristics (behaviour pressure and velocity fields), one can simply use the Navier–Stokes equations. In the remainder of the paper, we will use Navier–Stokes terminology as most readers are likely to be more familiar with its dynamics.

3. Homogeneous turbulence subject to periodic shear

There are important limitations to the types of time-varying mean velocity-gradient fields that can be generated in conjunction with homogeneous turbulence (Cambon & Scott 1999). However, many of these limitations can be overcome by introducing a suitable body force $\boldsymbol{F}(\boldsymbol{x}, t)$ in the momentum conservation equation. In this section, we present the strategy for generating and sustaining homogeneous turbulence subject to time-varying shear. We will then present the RANS and RDT equations for such a flow.

As a prelude to the periodic shear discussion, we first briefly examine the constant shear homogeneous turbulence generation. To facilitate comprehension, we develop

our strategy in the Navier–Stokes context and, subsequently, translate it to the lattice Boltzmann formulation. The Reynolds-averaged Navier–Stokes equation for the mean-velocity gradient is:

$$\frac{\partial}{\partial t}\frac{\partial U_i}{\partial x_j} + U_k\frac{\partial}{\partial x_k}\frac{\partial U_i}{\partial x_j} = -\frac{\partial}{\partial x_k}\frac{\partial\langle u_i u_k\rangle}{\partial x_j} - \frac{\partial U_k}{\partial x_j}\frac{\partial U_i}{\partial x_k} - \frac{\partial^2\overline{P}}{\partial x_i\partial x_j} + \nu\frac{\partial^2}{\partial x_k x_k}\frac{\partial U_i}{\partial x_j}, \quad (3.1)$$

where $\overline{P}$ is the mean pressure. To sustain a given steady spatially-uniform mean-velocity gradient in a homogeneous turbulent flow, the appropriate mean pressure field must be applied. This pressure field must satisfy the equation:

$$-\frac{\partial^2\overline{P}}{\partial x_i\partial x_j} = \frac{\partial U_k}{\partial x_j}\frac{\partial U_i}{\partial x_k}. \quad (3.2)$$

It is important to note that the left-hand side of (3.2) is a symmetric tensor and this considerably restricts the types of steady mean velocity gradients (right-hand side of the equation) that can be achieved with pressure field alone. Steady mean shear $(\partial U_i/\partial x_j = S\delta_{i1}\delta_{j2})$ is permitted and the pressure field required to generate it is:

$$-\frac{\partial^2\overline{P}}{\partial x_i\partial x_j} = \frac{\partial U_k}{\partial x_j}\frac{\partial U_i}{\partial x_k} = S^2\delta_{k1}\delta_{j2}\delta_{i1}\delta_{k2} = S^2\delta_{12}\delta_{j2}\delta_{i1} \equiv 0. \quad (3.3)$$

Thus, to sustain the initial homogeneous mean shear, a constant mean pressure gradient field is sufficient.

As mentioned earlier, to achieve complex time-varying mean flows, additional body force, $\boldsymbol{F}(\boldsymbol{x},t)$, is required. For this purpose we will consider a body force that is a function of space and time, but completely deterministic: $\boldsymbol{F}$ does not contain a fluctuating part. Now the mean and fluctuating velocity equations can be written as:

$$\frac{\partial U_i}{\partial t} + U_k\frac{\partial U_i}{\partial x_k} + \frac{\partial\langle u_i u_k\rangle}{\partial x_k} = -\frac{\partial\overline{P}}{\partial x_i} + F_i, \quad (3.4)$$

$$\frac{\partial u_i}{\partial t} + U_k\frac{\partial u_i}{\partial x_k} + \frac{\partial}{\partial x_k}(u_i u_k - \langle u_i u_k\rangle) = -\frac{\partial p'}{\partial x_i} - u_k\frac{\partial U_i}{\partial x_k} + \nu\frac{\partial^2 u_i}{\partial x_k\partial x_k}. \quad (3.5)$$

The Poisson equation for mean and fluctuating pressure (p') fields are:

$$\frac{\partial^2\overline{P}}{\partial x_k\partial x_k} = -\frac{\partial U_j}{\partial x_k}\frac{\partial U_k}{\partial x_j} + F_{k,k} - \frac{\partial\langle u_i u_k\rangle}{\partial x_i\partial x_k}, \quad (3.6)$$

$$\frac{\partial^2 p'}{\partial x_k\partial x_k} = -2\frac{\partial U_j}{\partial x_k}\frac{\partial u_k}{\partial x_j} - \frac{\partial u_j}{\partial x_k}\frac{\partial u_k}{\partial x_j} + \frac{\partial\langle u_i u_k\rangle}{\partial x_i\partial x_k}. \quad (3.7)$$

It is clear that the fluctuating velocity and pressure field equations are unaffected by the forcing, provided the force is purely deterministic. Now the mean velocity-gradient evolution equation can be written as

$$\frac{\partial}{\partial t}\frac{\partial U_i}{\partial x_j} + U_k\frac{\partial}{\partial x_k}\frac{\partial U_i}{\partial x_j} = -\frac{\partial}{\partial x_k}\left(\frac{\partial\langle u_i u_k\rangle}{\partial x_j}\right) - \frac{\partial U_k}{\partial x_j}\frac{\partial U_i}{\partial x_k} - \frac{\partial^2\overline{P}}{\partial x_i\partial x_j} + \nu\frac{\partial^2}{\partial x_k x_k}\frac{\partial U_i}{\partial x_j} + F_{i,j}. \quad (3.8)$$

If the Reynolds stress and the mean velocity gradient are uniform in space, the equation reduces to

$$\frac{\partial}{\partial t}\frac{\partial U_i}{\partial x_j} = -\frac{\partial U_k}{\partial x_j}\frac{\partial U_i}{\partial x_k} - \frac{\partial^2\overline{P}}{\partial x_i\partial x_j} + F_{i,j}. \quad (3.9)$$

To sustain a spatially-constant velocity gradient, $F_{i,j}$ and $\partial^2 \overline{P}/(\partial x_i \partial x_j)$ must be uniform in space.

In summary, to achieve a time-varying mean velocity gradient acting on homogeneous turbulence, a body force with the following properties must be included:

(*a*) A deterministic force with no fluctuations;

(*b*) A force that is a linear function of space with the temporal dependence dictated by the time-variation of the desired mean velocity gradient;

(*c*) A force that satisfies equations (3.6) and (3.9).

The time-dependent mean velocity gradient of interest here is periodic shear of the type:

$$\frac{\partial U_i}{\partial x_j}(t) = S_{max} \sin(\omega t)\delta_{i1}\delta_{j2}, \tag{3.10}$$

The maximum value of the periodic shear is S_{max} and its numerical value in our computations is $S_{max} = 0.0006875$. It is easy to establish that the corresponding pressure field must satisfy

$$\frac{\partial^2 \overline{P}}{\partial x_k \partial x_k} = -\frac{\partial U_j}{\partial x_k}\frac{\partial U_k}{\partial x_j} + F_{k,k} = F_{k,k}. \tag{3.11}$$

To accomplish the required mean velocity gradient, without violating the homogeneity of the fluctuating field, the body force must satisfy equations (3.9) and (3.11). Now let us consider a body force of the type

$$\boldsymbol{F} = \omega S_{max}(y - y_{ref}) \cos(\omega t)\boldsymbol{i}, \tag{3.12}$$

where $\boldsymbol{i}$ is the unit vector along the x-direction. Also, (x, y) corresponds to (x_1, x_2) directions and y_{ref} is a reference point which we take to be at the centre of the computational domain. We will now demonstrate that this body force produces the required time-varying mean velocity gradient. Substitution of this body force in equation (3.11) yields

$$\frac{\partial^2 \overline{P}}{\partial x_k \partial x_k} = F_{k,k} = 0. \tag{3.13}$$

Thus the pressure gradient in this case is uniform in space, as in the constant shear case. For such a pressure field, we will have

$$\frac{\partial}{\partial t}\frac{\partial U_i}{\partial x_j} = -\frac{\partial^2 \overline{P}}{\partial x_i \partial x_j} + F_{i,j} = F_{i,j} = \omega S_{max} \cos(\omega t)\delta_{i1}\delta_{j2}. \tag{3.14}$$

The resulting mean velocity gradient can be easily shown to be identical to the required form given in equation (3.10). This confirms that the applied body force results in the desired time-dependent mean velocity gradient, while maintaining the fluctuating field statistically homogeneous in space. It is important to note that the temporal variation is not due to the pressure field. Finally, the mean velocity field in our computation is

$$U(y, t) = S_{max}(y - y_{ref}) \sin(\omega t). \tag{3.15}$$

The next step is to introduce the requisite body force in the LBM equation. The effect of body force can be achieved by the inclusion of an extra term in (2.3) (Guo, Zheng & Shi 2002):

$$f_\alpha(\boldsymbol{x}_i + \boldsymbol{e}_\alpha \delta t, t + \delta t) - f_\alpha(\boldsymbol{x}_i, t) = -\frac{1}{\tau}\left[f_\alpha(\boldsymbol{x}_i, t) - f_\alpha^{(eq)}(\boldsymbol{x}_i, t)\right] + \delta t G_\alpha, \tag{3.16}$$

where

$$G_\alpha = \left(1 - \frac{1}{2\tau}\right) w_\alpha \left[\frac{e_\alpha - V}{c_s^2} + \frac{e_\alpha \cdot V}{c_s^4} e_\alpha\right] \cdot F. \tag{3.17}$$

Equation (3.16) is the one which we solved in our numerical simulation.

3.1. *Reynolds-averaged Navier–Stokes equation*

For any arbitrary incompressible turbulent flow, the Reynolds-stress evolution equation can be written as

$$\frac{\bar{D}}{\bar{D}t} \langle u_i u_j \rangle + \frac{\partial}{\partial x_k} T_{kij} = P_{ij} + R_{ij} - \varepsilon_{ij}, \tag{3.18}$$

where

$$\frac{\bar{D}}{\bar{D}t} \equiv \frac{\partial}{\partial t} + U_j \frac{\partial}{\partial x_j} \tag{3.19}$$

is the mean substantial derivative and the turbulent transport of the Reynolds stress (T_{kij}) can be decomposed as

$$T_{kij} = T_{kij}^{(u)} + T_{kij}^{(p)} + T_{kij}^{(v)}.$$

In the above,

$$T_{kij}^{(u)} \equiv \langle u_i u_j u_k \rangle, \quad T_{kij}^{(v)} \equiv -v \frac{\partial \langle u_i u_j \rangle}{\partial x_k}, \quad T_{kij}^{(p)} \equiv \frac{1}{\rho} \langle u_i p' \rangle \delta_{jk} + \frac{1}{\rho} \langle u_j p' \rangle \delta_{ik}.$$

Production, pressure redistribution and dissipation are, respectively:

$$P_{ij} \equiv -\langle u_i u_k \rangle \frac{\partial U_j}{\partial x_k} - \langle u_j u_k \rangle \frac{\partial U_i}{\partial x_k}, \tag{3.20}$$

$$R_{ij} \equiv -\left\langle \frac{p'}{\rho} \left(\frac{\partial u_i}{\partial x_j} + \frac{\partial u_j}{\partial x_i}\right)\right\rangle, \tag{3.21}$$

$$\varepsilon_{ij} \equiv 2v \left\langle \frac{\partial u_i}{\partial x_k} \frac{\partial u_j}{\partial x_k}\right\rangle. \tag{3.22}$$

In homogeneous turbulence, the evolution equation simplifies to

$$\frac{\partial}{\partial t} \langle u_i u_j \rangle = P_{ij} + R_{ij} - \varepsilon_{ij}. \tag{3.23}$$

For homogeneous shear flow, these equations can be written in the componential form as:

$$\frac{\partial}{\partial t} \langle u_1 u_1 \rangle = -\langle u_1 u_2 \rangle \frac{\partial U_1}{\partial x_2} - \left\langle 2\frac{p'}{\rho} \frac{\partial u_1}{\partial x_1}\right\rangle - 2v \left\langle \frac{\partial u_1}{\partial x_k} \frac{\partial u_1}{\partial x_k}\right\rangle, \tag{3.24}$$

$$\frac{\partial}{\partial t} \langle u_2 u_2 \rangle = -\left\langle 2\frac{p'}{\rho} \frac{\partial u_2}{\partial x_2}\right\rangle - 2v \left\langle \frac{\partial u_2}{\partial x_k} \frac{\partial u_2}{\partial x_k}\right\rangle, \tag{3.25}$$

$$\frac{\partial}{\partial t} \langle u_3 u_3 \rangle = -\left\langle 2\frac{p'}{\rho} \frac{\partial u_3}{\partial x_3}\right\rangle - 2v \left\langle \frac{\partial u_3}{\partial x_k} \frac{\partial u_3}{\partial x_k}\right\rangle, \tag{3.26}$$

$$\frac{\partial}{\partial t} \langle u_1 u_2 \rangle = -\langle u_2 u_2 \rangle \frac{\partial U_1}{\partial x_2} - \left\langle \frac{p'}{\rho} \left(\frac{\partial u_1}{\partial x_2} + \frac{\partial u_2}{\partial x_1}\right)\right\rangle - 2v \left\langle \frac{\partial u_1}{\partial x_k} \frac{\partial u_2}{\partial x_k}\right\rangle. \tag{3.27}$$

It is important to note that the body force does not enter the Reynolds-stress equation as it acts only on the mean flow. Thus, the form of these RANS equations is independent of whether the shear is steady or time-varying.

3.2. *RDT equations for the fluctuating velocity field*

One of the objectives of our work is to compare the DNS results with inviscid RDT (rapid distortion theory) and RANS model calculations. A detailed description of RDT can be found in standard text-books (Pope 2000). In a variety of flows, including rotating homogeneous shear and elliptic streamline flows, RDT has proved to be very accurate at capturing important characteristics of turbulence behaviour observed in experimental and numerical experiments. Rapid distortion theory entails the analysis of the linearized Navier–Stokes equations and, hence, excludes nonlinear effects. Comparison of RDT and DNS results will provide clear insight into the roles of linear and nonlinear turbulence dynamics in this flow.

At high Reynolds numbers, the linear effects of production and pressure–strain correlation are most prominent at the large scales, while the viscous action occurs in the small scales of motion. The two effects are separated by the inertial scales of motion in which the nonlinear cascading mechanism is of prime importance. Thus, the cascade due to the nonlinear effects completely changes the way in which viscous effects manifest on turbulence. In a typical high-Reynolds-number flow, the linear turbulence physics is completely unaffected by viscous action. Therefore, we will perform inviscid RDT and then will conjecture on the effect of viscosity.

The governing equations at the inviscid RDT limit are obtained by omitting nonlinear and viscous terms in the fluctuating velocity (3.5) and pressure (3.6) equations leading to:

$$\left.\begin{aligned}
\frac{\overline{D}u_i}{\overline{D}t} &= -\frac{\partial p'}{\partial x_i} - u_k \frac{\partial U_i}{\partial x_k}, \\
\frac{\partial^2 p'}{\partial x_k \partial x_k} &= -2\frac{\partial U_j}{\partial x_k}\frac{\partial u_k}{\partial x_j}.
\end{aligned}\right\} \tag{3.28}$$

It is important to note that the form of these fluctuating equations is completely unaffected by the forcing or the time-variations in the mean velocity gradients. Therefore, to perform RDT simulations of the present flow field, the standard RDT approach can be used.

In the standard approach, the RDT governing equations are solved in Fourier space (wavenumber $\boldsymbol{\kappa}$) in a coordinate frame that is moving with the mean velocity field. For this reason, the wavenumber of each fluctuating mode itself changes in time. Because of the linearity of the RDT equations, the amplitudes of velocity ($\hat{\boldsymbol{u}}(\boldsymbol{\kappa}, t)$) and pressure ($\hat{p}(\boldsymbol{\kappa}, t)$) of each mode evolve independently of those of others. The evolution equations for the wavenumber $\boldsymbol{\kappa}(t)$ and velocity amplitude $\hat{\boldsymbol{u}}(t)$ of each mode are given by (Townsend 1976):

$$\frac{d\kappa_l}{dt} = -\kappa_j \frac{\partial U_j}{\partial x_l}(t), \tag{3.29}$$

$$\frac{d\hat{u}_j}{dt} = -\hat{u}_k \frac{\partial U_l}{\partial x_k}(t)\left(\delta_{jl} - 2\frac{\kappa_j \kappa_l}{\kappa^2}\right). \tag{3.30}$$

It can be easily seen that the velocity amplitude and wavenumber of each mode satisfy the incompressibility condition:

$$\hat{u}_i \kappa_i = 0. \tag{3.31}$$

Equations (3.29)–(3.30) form the basis of our RDT calculations.

The RDT Reynolds stress equation is obtained by summing correlations over all fluctuating modes:

$$\frac{\partial}{\partial t}\langle u_i u_j\rangle = -\langle u_j u_k\rangle\frac{\partial U_i}{\partial x_k} - \langle u_i u_k\rangle\frac{\partial U_j}{\partial x_k} + 2\frac{\partial U_l}{\partial x_k}(M_{kjil} + M_{ikjl}). \qquad (3.32)$$

In (3.32), M_{ijkl} is a fourth-order tensor defined by

$$M_{ijkl} = \sum \hat{u}_i^* \hat{u}_j \frac{\kappa_k \kappa_l}{\kappa^2}, \qquad (3.33)$$

where $*$ is the complex conjugate. The RDT (rapid) pressure–rate-of-strain tensor $R_{ij}^{(r)}$ can be identified as

$$R_{ij}^{(r)} = 2\frac{\partial U_l}{\partial x_k}(M_{kjil} + M_{ikjl}). \qquad (3.34)$$

Finally, the RDT Reynolds-stress evolution, (3.32), can be rewritten in the simple form

$$\frac{\partial}{\partial t}\langle u_i u_j\rangle = P_{ij} + R_{ij}^{(r)}. \qquad (3.35)$$

Therefore, in RDT, Reynolds-stress evolution is governed entirely by the linear processes of production and rapid pressure–strain correlation. Remember that the mean velocity-gradient can be time-varying in all the above equations.

4. Computational methodology validation

In Navier–Stokes DNS of homogeneous shear turbulence, the computational domain is typically a cube with periodic boundary conditions imposed in all directions for the fluctuating fields. The computation is performed on a grid moving with the mean flow (the so-called Rogallo coordinates). The shear deforms this grid and remeshing must be frequently performed (Rogallo 1981). The mean velocity gradient appears as a forcing term in the fluctuation equation and can be simply specified to be a constant.

In laboratory experiments, flows are contained within walls and homogeneous turbulence measurements are made in the core portion of a bounded flow, before the wall influences penetrate the region of interest. In our LBM-DNS, we adopt a computational domain which is similar to the one in experiments. The computational domain is bounded in flow-normal direction (y-direction in figure 1) by frictionless walls and periodic boundary conditions are employed in streamwise (x) and spanwise (z) directions. This computational domain is exactly the same as the one employed by Schumacher & Eckhardt (2000) in their Navier–Stokes based DNS. In the y-direction, the presence of the walls and the resulting pressure-blockage and viscous effects will lead to inhomogeneity. The inhomogeneous effects will start at the wall and propagate toward the core of the flow. This will also be the case in any laboratory experiment of homogeneous flows. As in experiments, we will gather statistics in the core region of the flow before the wall effects compromise the homogeneity of the turbulence field. The grid resolution is 128^3 and to avoid wall effects, the statistics are gathered only in the core-region of $128 \times 64 \times 128$ as shown in figure 1. This arrangement is a variant of the Couette-flow boundary conditions employed in our previous work with constant-shear forcing (Yu & Girimaji 2005). The new set-up is more readily amenable to periodic forcing. In this section, we seek to achieve two objectives: to confirm homogeneity in the constant-shear case; and, to demonstrate that homogeneity is preserved in the periodic shear case as well.
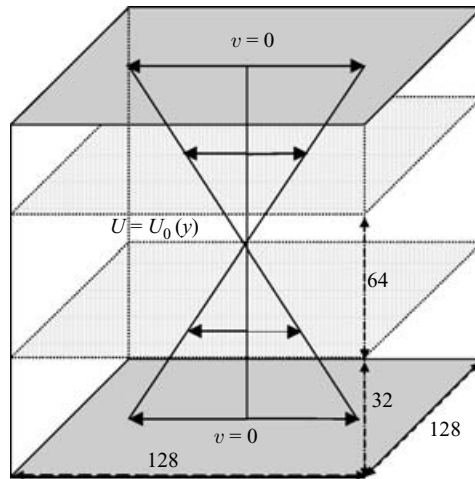
FIGURE 1. Computational domain. The statistics are obtained in the core region of the computational domain which is $128 \times 64 \times 128$.

4.1. *Validation in constant shear case*

We first establish the initial flow field: an isotropic fluctuating velocity field superposed on a constant shear mean velocity field. Three stages are involved in establishing this flow field. First, a random isotropic fluctuating field is generated in the computational domain using standard techniques (Yu *et al.* 2005). Next, we let this turbulence decay for about one eddy turnover time to achieve close consistency with the initial spectrum of case RR128 by Rogers (1986). Finally, the mean velocity ($S = \partial U / \partial y$) is added to the fluctuating velocity. In our simulations, the initial Taylor Reynolds number is $Re_\lambda = 33$ and initial non-dimensional shear is $S^* = 3.3$. In our computational set-up, as clearly demonstrated in the previous section, no external forcing is necessary to sustain the initially prescribed constant shear in regions away from the wall.

In LBM-DNS simulations of the total velocity field, it is necessary to ensure that the uniformity of shear and homogeneity of the fluctuating field are maintained throughout the computations. We plot in figure 2 the mean velocity profile $U(y)/U_{max}$ at the final stage of computation ($St = 12$) and the turbulent kinetic energy distributions $k(y)/k$ at the initial and final stages of computation. In the figure, $U(y)$ is the average fluid velocity on a given (x, z)-plane and U_{max} is the initial maximum mean velocity in the domain. The linearity of the plane-averaged velocity clearly confirms the uniform shear is sustained throughout the computation. In the kinetic energy plot, $k(y)$ is the plane-averaged kinetic energy and k is the volume-averaged value. Initially, this value is nearly constant at all y-planes, confirming the homogeneity of the initial fluctuating field. At the final time-step, the plane-averaged kinetic energy is constant in the core of the flow, but drops off rapidly close to the walls. Clearly, the wall effects are significant on kinetic energy, but have not penetrated the core area ($32 \leqslant y \leqslant 96$) from which the statistics are calculated. Based on these results, we confirm that the required flow conditions are satisfied in our computations. Importantly, turbulence attains the all-important structural-stationarity state long before the wall effects are felt in the core portion of the domain.

It should be reiterated here that the frictionless (slip but no penetration) wall condition is employed in our computation. It was found that the no-slip boundary
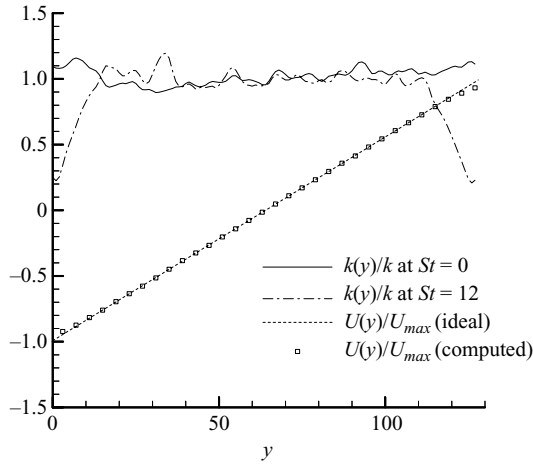
FIGURE 2. The profile of mean velocity at $St = 12$ and the distribution of $k(y)$ at the initial stage and $St = 12$. The wall effects are limited to regions near the walls. In the inner region, mean velocity agrees well with the ideal mean velocity and homogeneity of turbulence is maintained.
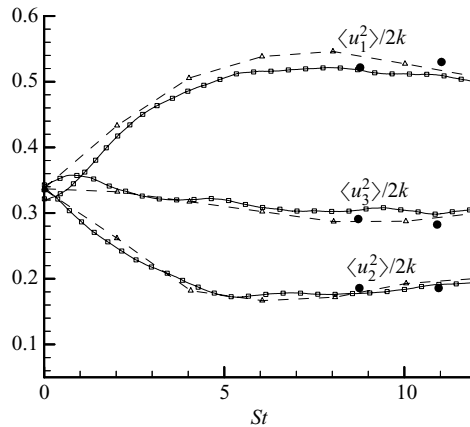

FIGURE 3. —□— Evolution of normal Reynolds stress in homogeneous turbulent shear flow (constant shear). —△— NS-DNS data are from Rogers (1986) with initial values of $Re_\lambda \approx 35$ and $S^* = 1.2$. ●,Experimental data are from Tavoularis & Corrsin (1981a) with $Re_\lambda = 284$ at $St = 8.6$.

condition leads to a more rapid penetration of the wall effects into the core portion of the flow.

As the final step of our constant-shear validation study, we compare the computed statistics against benchmark data of Tavoularis & Corrsin (1981a, b), Rogers (1986) and Jacobitz, Sarkar & Van Atta (1997). In figure 3, the time evolution (in normalized St units) of normal Reynolds stresses computed with LBM-DNS is compared against the NS-DNS data of Rogers (1986). Also shown are two near-asymptotic values from the experiments of Tavoularis & Corrsin (1981a). It is clear that LBM-DNS captures not only the asymptotic state, but also the transient evolution very well. In figure 4, the anisotropy shear component (b_{12}) evolution obtained from LBM-DNS is compared against the data from Jacobitz *et al.* (1997). The transient and asymptotic
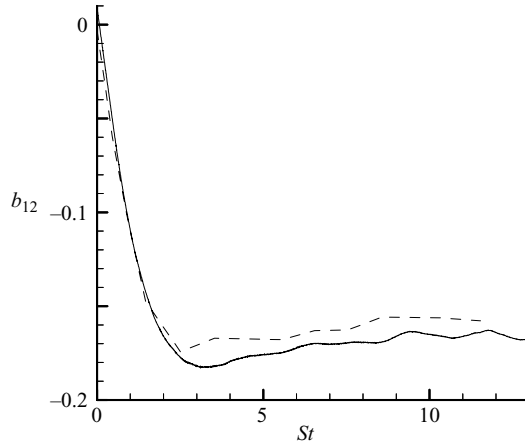
FIGURE 4. The results of b_{12} obtained from —, DNS using LBM and - - -, Navier–Stokes equations by Jacobitz, Sarkar & Van Atta (1997) with initial values of $Re_\lambda = 44.72$ and $Sk/\varepsilon = 2.0$.
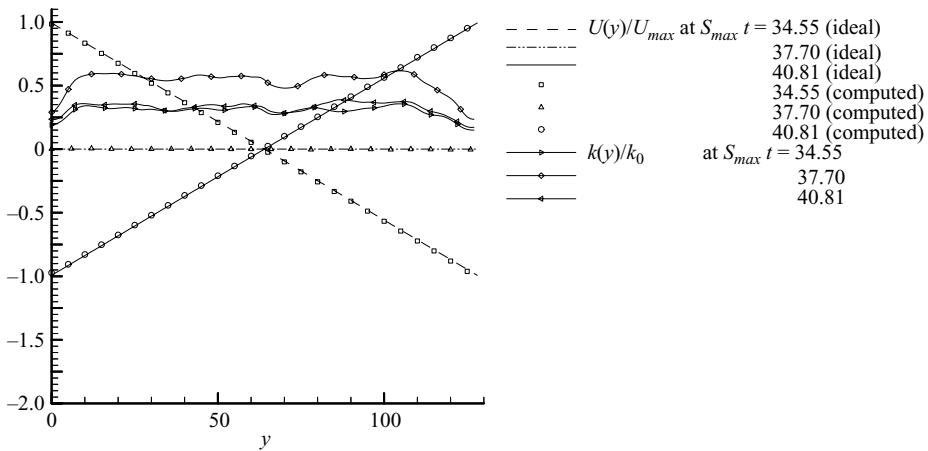

FIGURE 5. The profiles of $U(y)$ and $k(y)$ at $S_{max}t = 34.55$, 37.70, and 40.81 for $\omega/S_{max} = 0.5$. Ideal *vs.* computed.

behaviour are well captured by LBM-DNS. We conclude that LBM, with the current computational set-up, has the capability for extension to more complex flows.

4.2. *Validation in periodic shear case*

For achieving periodic shear, the requisite forcing, discussed in §3, is included and equation (3.16) is solved starting from an isotropic initial turbulent field. For a given value of ω ($\omega/S_{max} = 0.50$), we examine in detail the homogeneity of the turbulence field.

Streamwise (x) and spanwise (z) homogeneity are guaranteed by enforcing period boundary conditions in those directions. We will again examine the dependence on plane-averaged statistics (moments averaged over (x, z)-planes) as a function of the wall-normal distance y.

Figure 5 shows the mean velocity profiles $U(y)/U_{max}$ and the turbulent kinetic energy distributions $k(y)/k_0$ at $S_{max}t = 34.55$, 37.70 and 40.81. At the times shown,
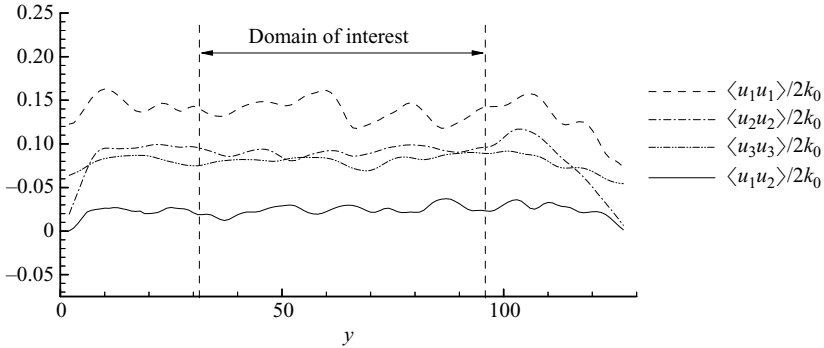
FIGURE 6. Planar-averaged Reynolds stresses along the y-direction at $S_{max}t = 34.55$.
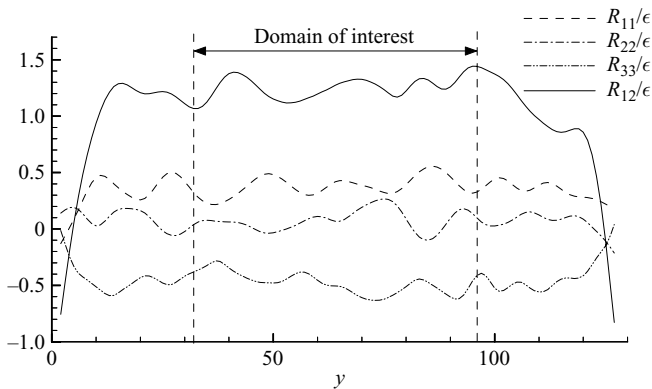

FIGURE 7. Planar-averaged pressure–strain correlations along the y-direction at $S_{max}t = 34.55$.

the desired shear is at its negative maximum, zero and positive maximum states, respectively. We can see that computed mean velocity in figure 5 agrees with desired linear profiles very well even in regions near the lower and upper walls. However, the walls have relatively larger effects on the turbulence field, as shown in the same figure. In the region of interest ($32 \leqslant y \leqslant 96$), homogeneity is well preserved. We probe further and examine y-dependence of all of the turbulence moments in the Reynolds-stress evolution equation. For the case of homogeneous (steady or unsteady) shear turbulence these equations reduce to a balance between production, dissipation and pressure–strain correlation (see (3.24)–(3.27)). The production involves the mean velocity gradients and Reynolds stresses. To prove homogeneity conclusively, we then need to show that the various components of Reynolds stress, dissipation and pressure–strain correlation are independent of y.

The plane-averaged components of Reynolds stresses, pressure–strain correlation and dissipation are plotted in the figures 6, 7 and 8 at $S_{max}t = 34.75$. The Reynolds stresses are normalized by the initial kinetic energy k_0, and the pressure–strain correlation and dissipation are normalized by magnitude of dissipation tensor ϵ_{ii} at $S_{max}t = 34.75$. Overall, homogeneity is reasonably well preserved, even with the high-order moments in the core area. The pressure–strain exhibits slightly larger excursions from the mean than the other terms. This variation can be attributed to statistical uncertainty, rather than violation of homogeneity, as there is no clear trend in y-dependence. It should also be noted that LBM is a compressible scheme, in
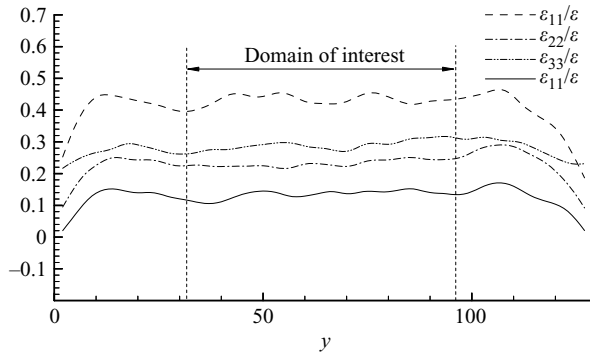
FIGURE 8. Planar-averaged components of the dissipation tensor along the y-direction at $S_{max}t = 34.55$.

which speed of sound is finite and pressure is determined from the equation of state. Thus, the pressure oscillations due to presence of the wall can be much more localized than in an incompressible solver. In our computations, we use both single-relaxation time (SRT) and multi-relaxation time (MRT) LBM models. The introduction to the SRT model is given in §2. For a discussion of the MRT model, see d'Humières *et al.* (2002). For lower-order statistics, MRT and SRT computations yielded comparable results. For higher-order moments, MRT was found to be superior. All the results presented in this sub-section are from MRT computations.

As the final confirmation of homogeneity, we also compute the turbulent transport terms T_{ijk}. It is found that the transport is an order of magnitude smaller than pressure-correlation terms. Thus it can be concluded that the turbulence field is indeed homogeneous as desired.

5. DNS results

The effects of six different forcing frequencies on turbulence evolution are studied: $\omega/S_{max} = 0.125, 0.25, 0.50, 0.75, 1.0$ and 10. In all the cases, the initial turbulence field is isotropic and prepared as described in §4 and allowed to evolve according to (3.16). The various statistical moments are computed as a function of time. The results are sorted into several different categories: kinetic energy and dissipation; production; shear anisotropy; normal anisotropy; Reynolds stress budget; and limiting high-frequency behaviour. Each category is examined individually and in relation with other categories.

5.1. *Evolution of k and ε*

In all the cases studied, turbulence decays initially as the production is nearly zero (due to Reynolds stress isotropy) and dissipation is comparatively large. After the initial decay, subsequent evolution of k is different for different frequencies as shown in figure 9. In $\omega/S_{max} = 0.125$ and 0.25 cases, k grows rapidly after the initial period of decay. The growth, however, is not monotonic and cyclic variations from the mean trend are very much in evidence. In the case of $\omega/S = 0.5$, the initial decay period is followed by a long period of purely periodic behaviour. Beyond $S_{max}t \approx 25$, the kinetic energy shows signs of very slow growth. In $\omega/S_{max} = 0.75$ and 1.0 cases, k appears to decay with each cycle of applied strain. It is clear that two distinct turbulence responses are possible depending on the frequency of forcing. At low shear frequencies, turbulence grows at long times, although not necessarily monotonically. At high shear
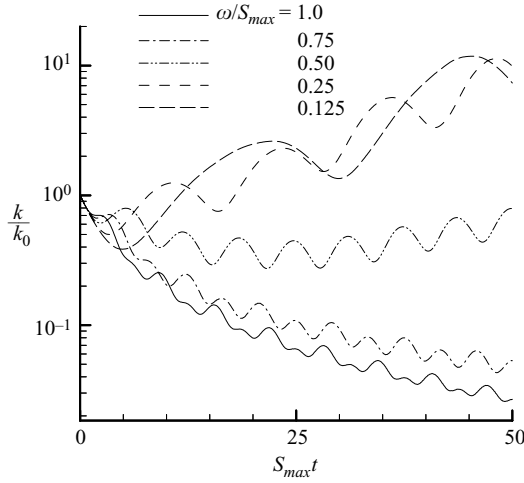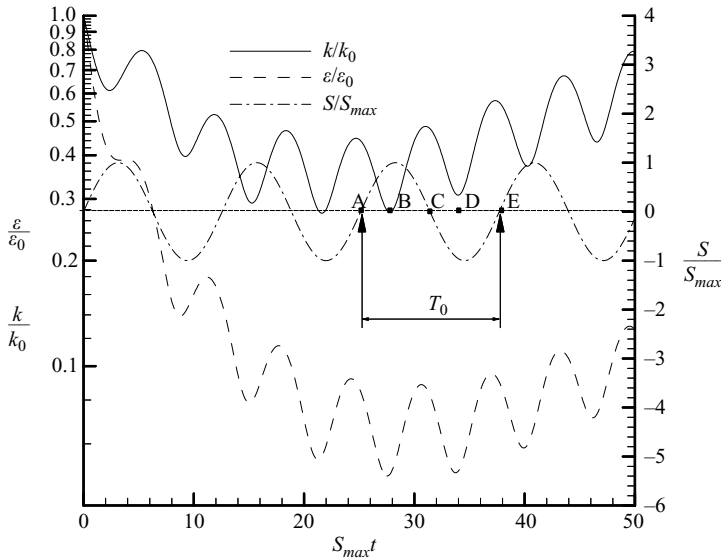
FIGURE 9. Evolution of k in various ω/S_{max} cases.

FIGURE 10. Evolution of k and ε in the $\omega/S_{max} = 0.5$ case.

frequencies, turbulence decays. The switch from turbulence decay to growth occurs at a frequency of approximately $\omega/S_{max} = 0.5$. It is likely that at some normalized frequency close to 0.5, turbulence neither decays or grows. It is, however, difficult to precisely pin-point this value frequency for which the turbulence level remains close to its initial condition. While the turbulence dynamics in the growth cases are likely to be similar to the steady forcing case, the physics of the decaying cases require further investigation.

Two decaying cases ($\omega/S_{max} = 0.5$ and 1.0) are studied in more detail in figures 10 and 11. In these figures, the cycles of k variation are compared to those of S-variation and the behaviour of dissipation is also examined. Clearly, the frequency of variation k is twice that of shear. We identify five points in time (A, B, C, D and E) in one period
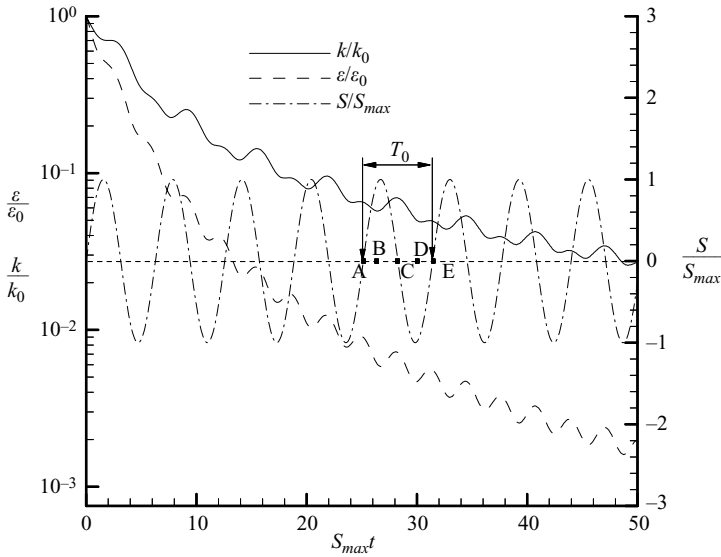
FIGURE 11. Evolution of k and ε in the $\omega/S_{max} = 1.0$ case.

(T_0) of shear cycle. Points A, C and E correspond to consecutive zero-crossing times of S and points B and D correspond the consecutive minima times in k variation. In the $\omega/S_{max} = 1.0$ case, consecutive k peaks have progressively smaller magnitudes indicating decay. In the $\omega/S_{max} = 0.5$ case, consecutive peaks in the intermediate period of evolution are nearly identical.

In all the cases considered, the evolution cycles of k and ε are in phase. This observation has important modelling implications. The current closure strategy of modelling production of dissipations in terms of production of kinetic energy appears to be valid for time-dependent forcing as well, at least at these low Reynolds numbers.

5.2. *Time dependence of* P/ε

A simple examination of the kinetic energy equation in homogeneous flows

$$\frac{\mathrm{d}k}{\mathrm{d}t} = P - \varepsilon, \tag{5.1}$$

reveals that k-evolution is completely dictated by the difference between production and dissipation. In order to understand the observed evolution of k, we investigate the behaviour of the P/ε ratio. This ratio must exceed unity for turbulence to grow.

Figures 12 and 13 show the evolution of P/ε. The evolution is generally oscillatory with periods of negative production. Negative production is rarely seen in turbulence subject to constant forcing, but may be important in many practical flows. Over the first half-cycle of forcing, strain and production are in phase and their frequencies appear to be the same. However, a phase difference soon develops and the frequency of the ratio (P/ε) quickly becomes twice that of the applied strain, as can be seen from monitoring the five reference points A, B, C, D and E (defined in figures 10 and 11). At all these points, production goes to zero. The zeros at A, C and E are due to the strain-rate going to zero. The zeros at B and D, as will be seen soon, are due to vanishing Reynolds stress component $\langle u_1 u_2 \rangle$. The frequency of the production cycle drives the kinetic energy cycle. Thus, the kinetic energy cycle is also twice that of the applied strain rate as seen previously. The cycle-averaged ratio
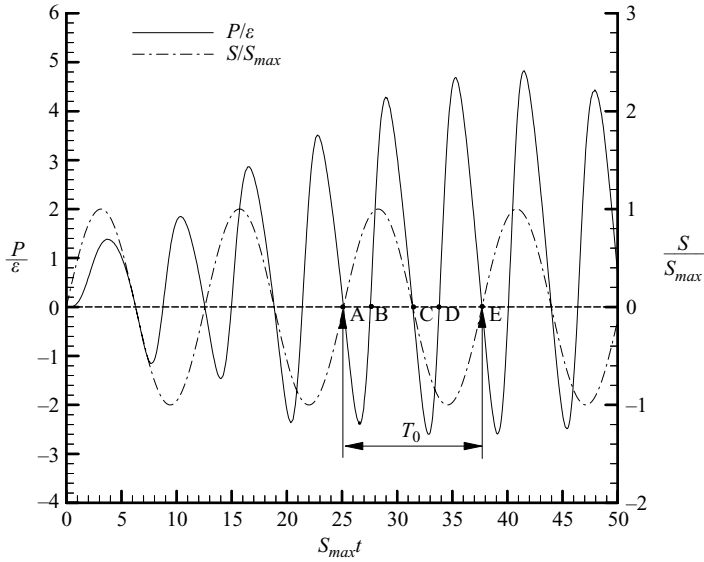
FIGURE 12. Evolution of production over dissipation ratio (P/ε) in the $\omega/S_{max} = 0.5$ case.
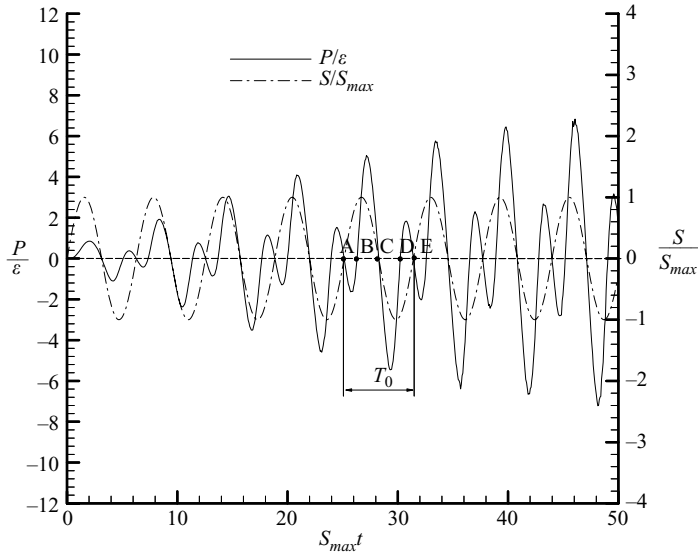

FIGURE 13. Evolution of production over dissipation ratio (P/ε) in the $\omega/S_{max} = 1.0$ case.

grows gradually beyond unity in the low-frequency cases: $\omega/S_{max} \leqslant 0.5$. At higher frequencies, the cycle-averaged ratio lingers around zero (e.g. the $\omega/S_{max} = 1$ case shown in figure 13). Thus, the observed k behaviour can be completely explained in terms of the asymptotic trends of mean production-to-dissipation ratio.

5.3. *Evolution of b_{12}*

To gain further insight into the behaviour of P/ε, we next examine the evolution of shear anisotropy b_{12}, which, in conjunction with $S(t)$, determines production. In constant shear turbulence, b_{12} and S are of opposite signs.
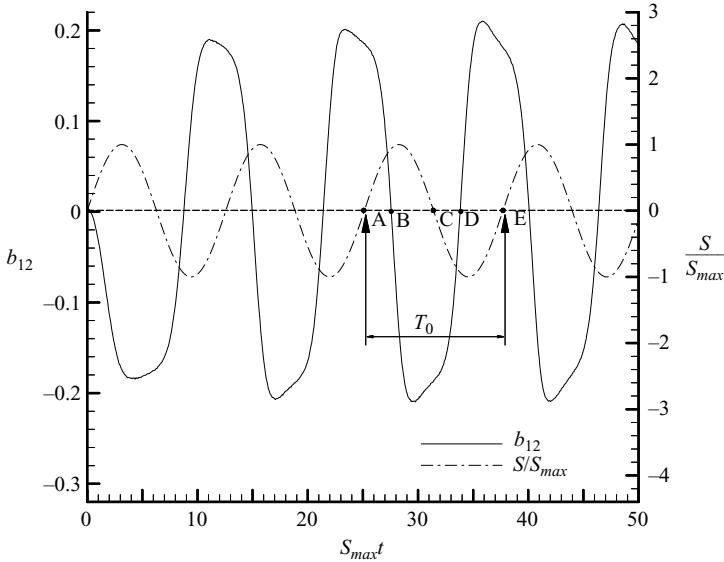
FIGURE 14. Evolution of b_{12} in the $\omega/S_{max} = 0.5$ case.

The evolution of anisotropy component b_{12} in the $\omega/S_{max} = 0.5$ case is shown in figure 14. The time variation of shear is also given in the figure. For the first quarter of the cycle, b_{12} is in phase with S and evolution is as expected. As the value of the applied strain begins to diminish after peaking, a phase lag develops. When the strain goes to zero at the half-cycle mark, the stress is clearly non-zero highlighting the hysteresis effect. For a substantial portion of the third quarter of the first cycle, stress and strain are of the same sign, implying that the production is now negative. Toward the end of the third quarter, the stress passes through zero and production becomes positive again. Throughout the fourth quarter of the first cycle, the stress and strain are of opposite signs. At the end of the first cycle, the stress does not return to zero. The phase-lag between stress and strain continues to grow for another cycle of applied strain. By the end of the second cycle, stress and strain lock into a constant phase difference and evolve at the same frequency. In this asymptotic state, the dynamics is again examined using the reference points A, B, C, D and E. We divide the A–E time period into four intervals: AB, BC, CD and DE, as shown in figure 14. Just before time A, the shear is negative, b_{12} is positive, and production is positive. In the period AB, shear becomes positive while b_{12} still maintains positive values. In this period, production is negative as shown in figure 12. The negative production is also reflected in the rapid fall of k during the same period in figure 10. It can be seen in figure 14 that shear and b_{12} are relatively small in period AB hence the negative production is relatively small in magnitude. After time B, production returns to positive values until time C. As seen in figure 14, concurrence of large shear and b_{12} values produces large positive production during period BC. During period CD and DE, we see the same kind of production behaviour as in periods AB and BC.

Figure 15 shows the evolution of b_{12} for the $\omega/S_{max} = 1.0$ case. The differences between the two cases are clearly evident. In $\omega/S_{max} = 1.0$ case, b_{12} is not initially symmetric about zero with the negative values being much larger than positive values. This is caused by the initial sign of the applied shear. In our simulation, the initial shear is positive leading to large initial negative values of b_{12} in the first half of the
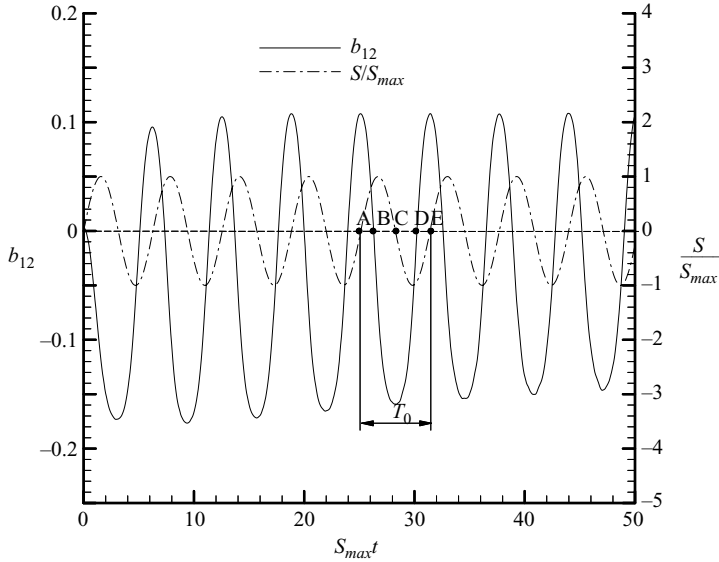
FIGURE 15. Evolution of b_{12} in the $\omega/S_{max} = 1.0$ case.

first cycle. At the second half of first cycle, the shear is negative and b_{12} is changing to positive values to keep in pace with the negative shear. However, before b_{12} can reach its full potential magnitude on the positive side, the first cycle rapidly comes to an end and the applied shear is positive again. Thus, the positive excursions of b_{12} are not as large initially as the negative excursions. With the passage of time, the bias toward negative values decreases as the effect of the initial sign of applied shear fades and the oscillations become more symmetric. Calculations with initial negative shear show the opposite initial bias, but do not change the observed asymptotic behaviour of the evolution of kinetic energy, production or dissipation.

The difference between the low- and high-frequency cases at long times is more important. Examining the time period A–E in the two cases, it can be seen that in the $\omega/S_{max} = 1.0$ case, period CD is much longer and period DE is much shorter than they are in the $\omega/S_{max} = 0.5$ case. This generates a large negative production during time CD and small positive production during time DE in the $\omega/S_{max} = 1.0$ case. Overall, the net production during a cycle can be judged by the lengths of AB + CD and BC + DE which correspond to the times when production has negative and positive values, respectively. If BC + DE is larger than AB + CD, net production will be positive. Otherwise, the cycle average of production will be negative. As b_{12} and S vary periodically, these lengths can be characterized by a single parameter: asymptotic phase lag (ϕ) between S and b_{12}. If $\pi/2 < \phi < \pi$, we will have (BC + DE) > (AB + CD), and the net production will be positive. If, on the other hand, $0 < \phi < \pi/2$, we will have (BC + DE) < (AB + CD), and the net production will be negative. If $\phi = \pi/2$, then (BC + DE) = (AB + CD), resulting in no net production in a cycle of applied strain. For the constant shear case, considering a constant shear as a pulse wave with infinite period, we have $\phi = \pi$. Thus, the production will always be positive. In our computations, the phase difference between stress and strain vary initially, but lock into a constant value at latter times. The dependence of the lock-in phase-lag as a function of the applied frequency is shown in figure 16. It is seen that phase lag goes from nearly π in the very low-frequency case to about $\pi/2$ in high-frequency cases.
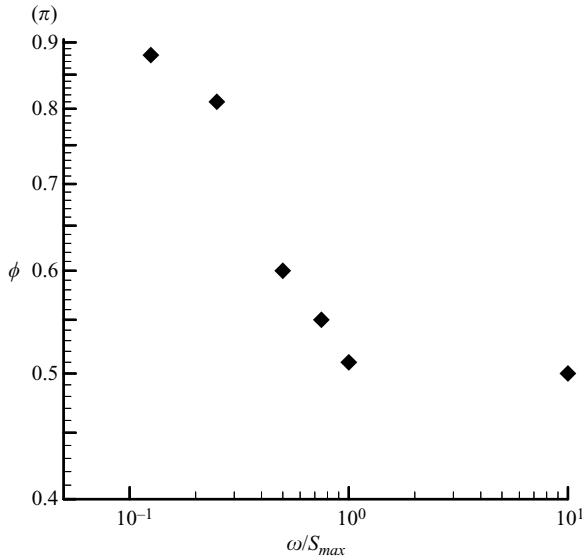
FIGURE 16. The dependence of phase lag ϕ on forcing frequency; the maximum and minimum values of ϕ are π and $\pi/2$, respectively.

Thus, the net production decreases with increasing frequency of forcing. The value of ϕ does not fall below $\pi/2$, implying that net production is always non-negative. Thus, the net energy transfer in each cycle is from the mean to the fluctuating field, except at very high frequencies at which the transfer goes to zero.

In order to sustain turbulence, the production must not only be positive, but must also exceed dissipation. From our computations, it appears that for $\omega/S_{max} > 0.5$, net cycle production is smaller than net cycle dissipation. We identify the critical frequency as $\omega_{cr} = 0.5S_{max}$, beyond which turbulence cannot be sustained. At higher frequencies, dissipation rate exceeds the rate at which energy is transferred from mean to fluctuating field.

5.4. *Normal anisotropy*

We now turn our attention to the normal components of Reynolds stress tensor. In homogeneous flows, these components play an important role in determining the secondary flow structures of the mean velocity field. The details of the evolution of the diagonal anisotropy components in $\omega/S_{max} = 0.5$, 0.65 and 1.0 cases are given in figures 17, 18 and 19. The major observations and their implications are now summarized.

The frequency of all normal (or diagonal) anisotropies is the same as that of kinetic energy and twice that of the applied shear or off-diagonal (b_{12}) anisotropy. This is to be expected as the frequency of kinetic energy is also twice that of shear due to the influence of production. That the diagonal Reynolds stress component should have twice the frequency off-diagonal component can also be understood from a second point of view. Considering one cycle of the evolution of $\langle u_1 u_2 \rangle$, we can expect $\langle u_1 u_1 \rangle$ and $\langle u_2 u_2 \rangle$, which are always positive, to attain their maximum values during the maximum positive or maximum negative value of $\langle u_1 u_2 \rangle$. The diagonal Reynolds stress will attain their minimum value when $\langle u_1 u_2 \rangle$ crosses zero. Thus, in the time that it takes the off-diagonal component to complete a half-cycle from maximum to minimum through zero, the diagonal components complete a full cycle.
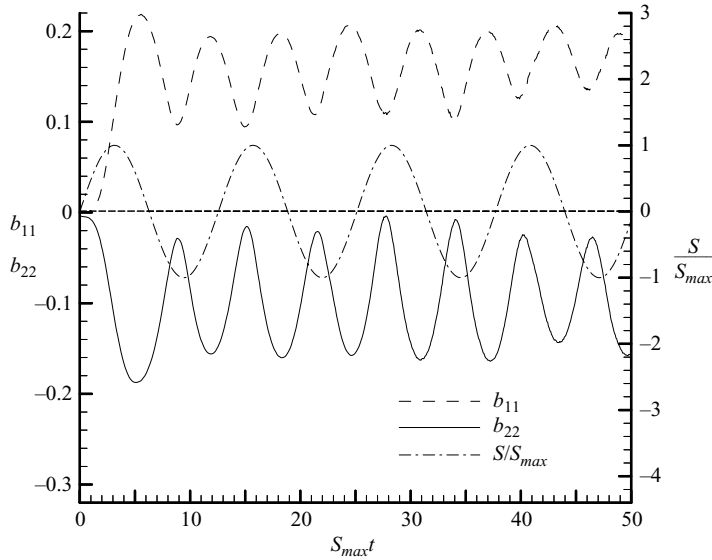
FIGURE 17. Evolution of b_{11} and b_{22} in the $\omega/S_{max} = 0.5$ case.
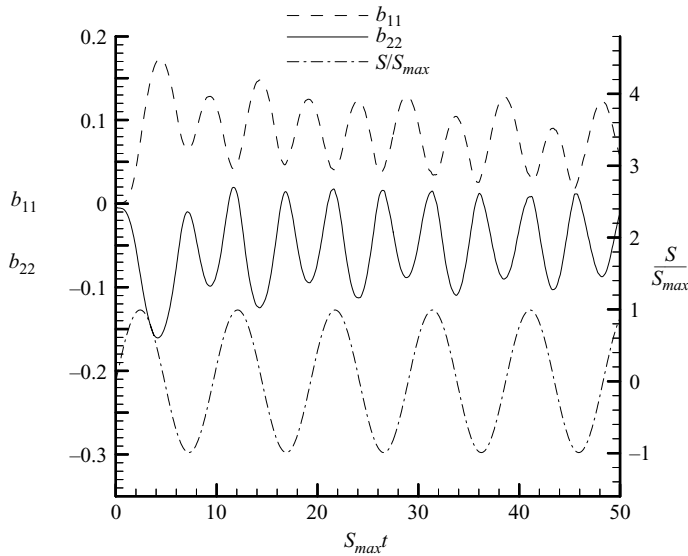
FIGURE 18. Evolution of b_{11} and b_{22} in the $\omega/S_{max} = 0.65$ case.

The difference in frequency between the applied strain and diagonal stresses also has important modelling implications. Approximations which imply that stress and strain have the same frequency will be invalid.

In the kinetic energy growth cases, the asymptotic cycle-mean anisotropy values are non-zero. For example, in the case of $\omega/S_{max} = 0.5$, the asymptotic cycle-mean values of b_{11} and b_{22} are about 0.15 and -0.1, respectively. In general, at all forcing frequencies, component b_{11} oscillates about a positive mean value and b_{22} about a negative value. The magnitude of the cycle-mean values of diagonal anisotropies decrease with increasing frequency. Thus, with increasing frequency, the diagonal
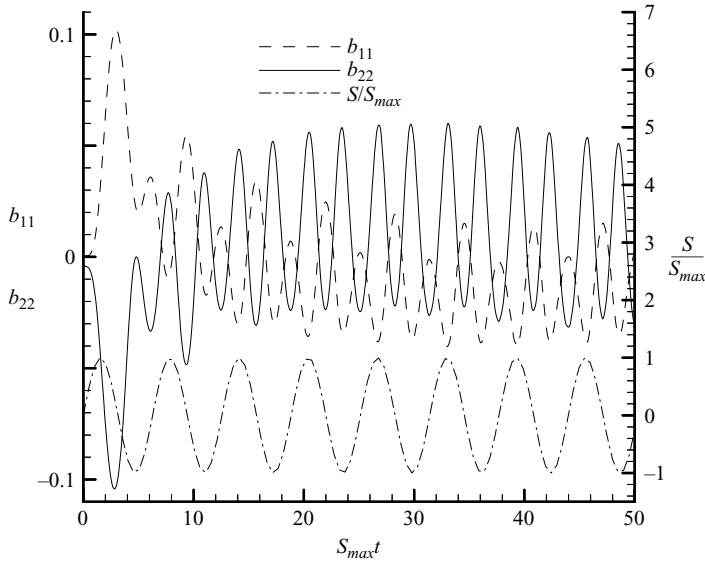
FIGURE 19. Evolution of b_{11} and b_{22} in the $\omega/S_{max} = 1.0$ case.

stresses tend closer toward the isotropic state. In all the decay cases, normal anisotropy tends to zero asymptotically, even if it develops non-zero values during the first cycle of shear. Thus, the decay cases evolve asymptotically to isotropic turbulence.

5.5. *Budget of Reynolds stress*

Reynolds-stress budgets offer more detailed insights into the physics of turbulence processes and are very important for high-order moment closure model development. We will now investigate the budgets of the various Reynolds stress components in the $\omega/S_{max} = 1.0$ case. Although the computations are performed with the lattice Boltzmann equation, the budgets will be discussed in the context of the Navier–Stokes equations. (The Reynolds stress budget equations are given in §3.) Following Pope (2000), production, pressure–strain correlation and dissipation are represented by P_{ij}, R_{ij} and ε_{ij}. Wherever possible, these budgets will be put in perspective with the budgets in constant shear homogeneous turbulence (Rogers 1986).

First and foremost, we must ensure that the numerical data is of high enough numerical accuracy that the various high-order derivatives and moments in the budgets can be computed with confidence. This is particularly important as the current computations employ a novel LBM approach rather than the tried and tested Navier–Stokes schemes. Figure 20 shows the comparison of the time derivative of Reynolds-stress $\langle u_1 u_1 \rangle$ computed from two independent means. One computation comes from summing the terms on the right-hand side of (3.24), each of which is first calculated independently. The second estimate of the time-derivative comes from the finite-difference operation on Reynolds-stress:

$$\frac{\mathrm{d}\langle u_i u_j \rangle}{\mathrm{d}t} = \frac{\langle u_i u_j(t + \mathrm{d}t) \rangle - \langle u_i u_j(t - \mathrm{d}t) \rangle}{2\delta t}.$$

The results from two different computations are indistinguishable. Further tests were performed to ensure the accuracy of other budget-term calculations (figures not shown). The results clearly indicate that all terms in the Reynolds-stress budget equation are adequately accurate.
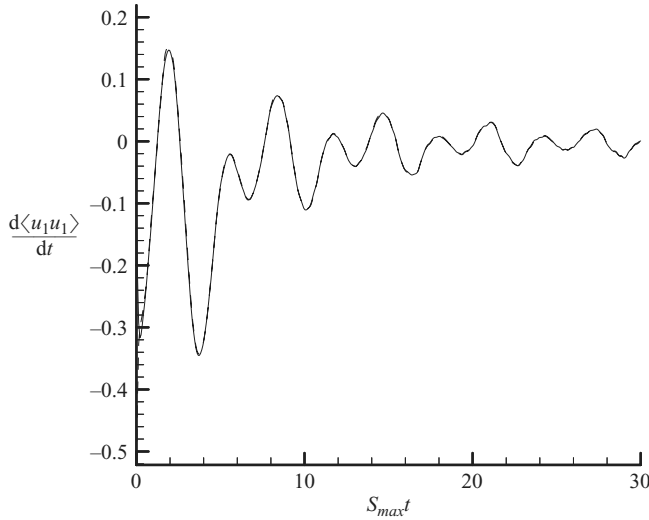
FIGURE 20. Comparison of $d\langle u_1 u_1 \rangle / dt$ computed from ——, numerical differentiation of $\langle u_1 u_1 \rangle$ and - - -, the right-hand side of (3.24) in the $\omega / S_{max} = 1.0$ case. $\langle u_1 u_1 \rangle$ is normalized by $\langle u_1 u_1 \rangle$ at $t = 0$.
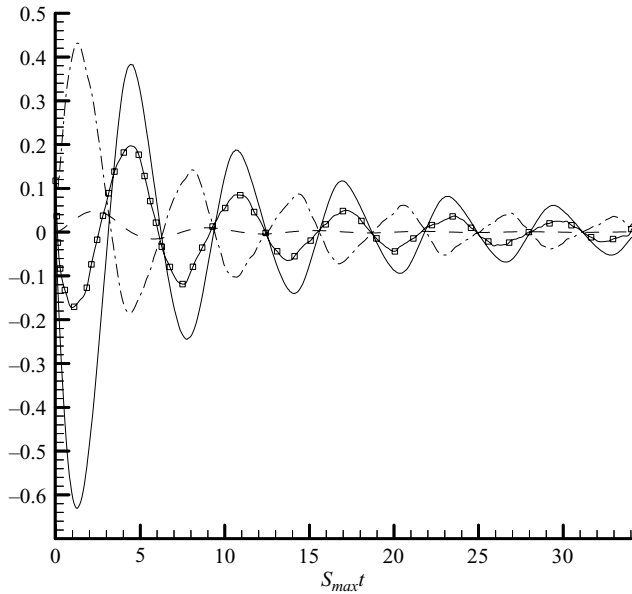

FIGURE 21. Temporal variation of the $\langle u_1 u_2 \rangle$ budget in the $\omega / S_{max} = 1.0$ case. ——, production; - - -, dissipation; —·—, pressure redistribution; —▱—, $d\langle v_1 v_2 \rangle / dt$. All terms are normalized by $\langle u_1 u_1 \rangle$ at $t = 0$.

Figure 21 shows different terms in the budget of $\langle u_1 u_2 \rangle$ evolution (equation (3.27)). The magnitudes of the various terms diminish with time as k decays from its initial value. As is to be expected in the case of off-diagonal stress, dissipation is quite small at all times. The pressure–strain distribution always counters production and the difference between the two drives the evolution. This balance is very similar to
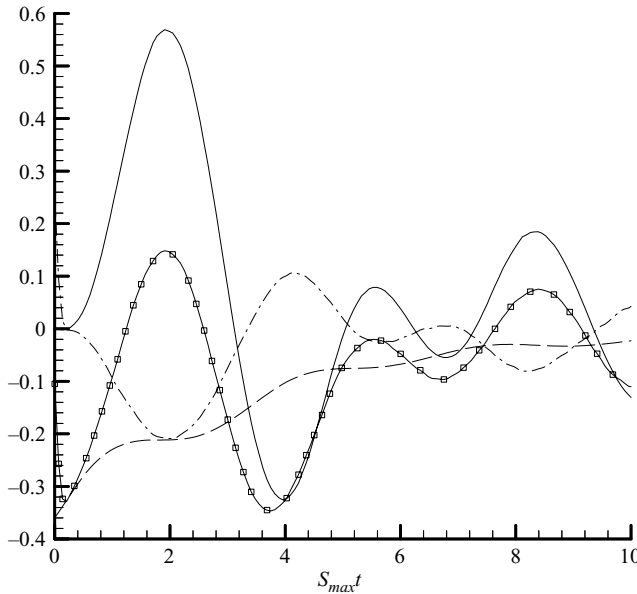
FIGURE 22. Early-time variation of the $\langle u_1 u_1 \rangle$ budget in the $\omega/S_{max} = 1.0$ case. Key as in figure 21.

that seen in the constant shear case (Rogers 1986), with the exception that production and pressure–strain distribution are now cyclic.

The budget of $\langle u_1 u_1 \rangle$ evolution is shown in figure 22. As in the case of constant shear, dissipation dominates the very early evolution ($S_{max} t \leqslant 1$) as the Reynolds-stress value falls rapidly. Although zero initially, production becomes the most dominant term soon ($S_{max} t > 1$). The peak value of normalized production in the time-varying and constant shear cases occur at the same normalized time: $S_{max} t = 2$. Pressure–strain redistribution almost always counters the effect of production, but there are rare instances when both the processes are of the same sign. It remains to be seen whether the current pressure–strain redistribution closures can capture this behaviour as most models assume that redistribution always counteracts production. At the intermediate stages ($1 \leqslant S_{max} t \leqslant 10$), the difference between production and the sum of dissipation and pressure–strain redistribution drives the evolution. At later stages, dissipation becomes negligible (in this decaying case).

The time dependence of budgets of $\langle u_2 u_2 \rangle$ and $\langle u_3 u_3 \rangle$ are quite similar and the latter budget is shown in figure 23. For both components, production is absent. Dissipation dominates the initial time ($S_{max} t \leqslant 3$) development, but quickly goes to zero thereafter. The later development is mainly due to pressure–strain redistribution. The production of $\langle u_1 u_1 \rangle$ is the only source of kinetic energy in this flow. We see that the magnitudes of production, the dissipation and redistribution decrease with time. The increase of the magnitude of P/ε in figure 13 is caused by the faster decrease of ε, rather than the increase of P.

Overall, it is clear that pressure redistribution plays a key role in determining the evolution of various normal components. Calculations were performed to confirm that the trace of the pressure–strain redistribution was indeed close to zero. Analysis of the three components reveals that R_{11} and R_{22} are nearly in phase, while the phase of R_{33} is shifted by nearly π. This means that energy is removed from $\langle u_1 u_1 \rangle$ and
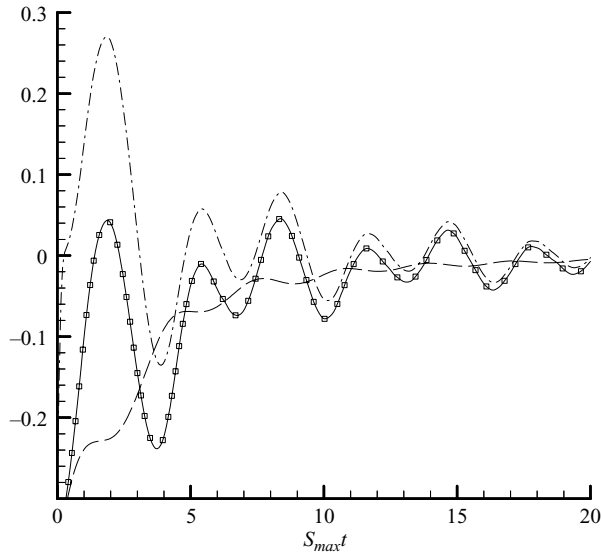
FIGURE 23. Time variation of the $\langle u_3 u_3 \rangle$ budget in the $\omega/S_{max} = 1.0$ case. Key as in figure 21.

$\langle u_2 u_2 \rangle$ and added to $\langle u_3 u_3 \rangle$. This is different from what is observed in constant shear homogeneous flow.

5.6. *Limiting high-frequency behaviour*

As mentioned in §1, the present flow shares some similarities with homogeneous shear flow in a rotating reference frame. For example, in both cases, turbulence grows when the frequency (of rotation or periodic variation) is small and decays when the frequency is large. However, there are very significant differences in the turbulence dynamics in the two cases. In the case of homogeneous shear flow in a rotating reference frame, turbulence tends to a two-componental limit at large rotation rates in keeping with the Taylor–Proudman theorem. Two-dimensionalization inhibits cascade (no vortex stretching) and diminishes production leading to viscous decay of the velocity field at all scales. In the present case, on the other hand, turbulence is isotropic at large frequencies of shear variation. The shear varies too rapidly to induce anisotropy and produce kinetic energy. We anticipate that at high frequencies, turbulence subject to rapidly varying shear will be more like decaying isotropic turbulence as net production will be insignificant. To establish that this is indeed the case, we will now compare the $\omega/S_{max} = 10$ case with decaying isotropic turbulence.

In the decaying isotropic turbulence simulation, all the initial conditions are the same as for homogeneous shear flow, except that the wall boundary condition is replaced by the periodic boundary condition and there is no mean shear in the flow. Figure 24 shows the evolution of k and ε for homogeneous shear and isotropic decaying cases. For consistency, time is normalized with S_{max}, although there is no shear in isotropic decay turbulence. In the homogeneous shear case, at the initial stage, k decays a little slower than in the isotropic decaying case; but overall, the decay rates are almost same for both cases. A similar examination of the dissipation rate demonstrates that the evolutions in the two cases are almost indistinguishable. The standard power-law decay is recovered in both cases. It must be pointed out that there are about 15 shear cycles in the period over which the comparison is made.
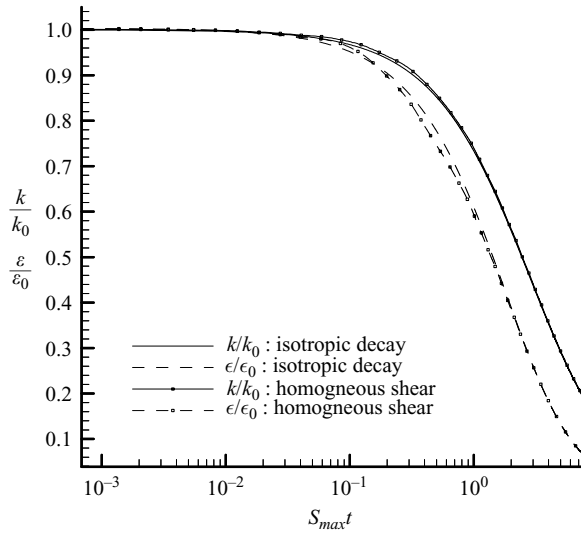
FIGURE 24. The evolutions of k and ε in isotropic decaying turbulence and homogeneous shear turbulence with $\omega/S_{max} = 10$.
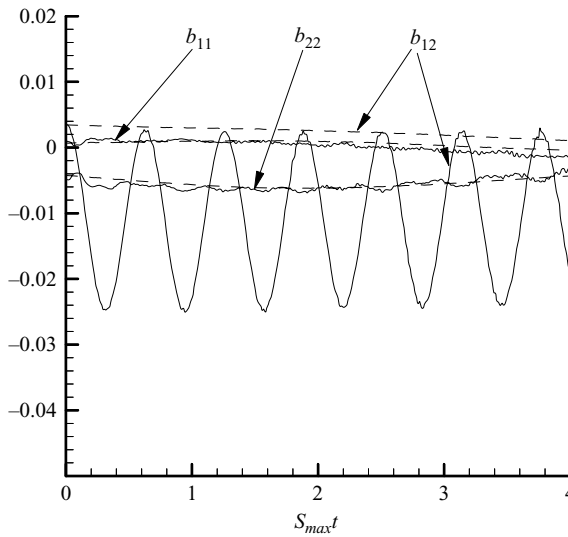

FIGURE 25. Evolution of the anisotropy tensor in $---$, isotropic decaying turbulence and —, homogeneous shear turbulence with $\omega/S_{max} = 10$.

Next we compare the evolution of anisotropy in the two cases in figure 25. The small level of anisotropy seen in the initial condition is due to finite statistical sample size. The time-development of the diagonal anisotropies in the decaying and high-frequency forcing cases are similar, with the latter exhibiting small-amplitude oscillations about the former. With regard to b_{12}, the difference between the two cases is discernible. The negative bias of b_{12} in the forced case has already been explained above. The most significant features are: the cycle-averaged b_{12} in the forced case is quite different from the b_{12} in the isotropic decaying case; and the amplitude of oscillation is sizeable. Despite the large amplitude of the b_{12} variation, the production
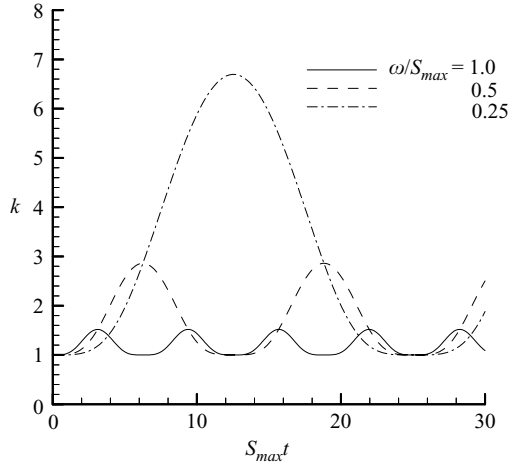
FIGURE 26. RDT evolution of k for $\omega/S_{max} = 0.25$, 0.5 and 1.0.

is very small because stress and strain are out of phase by $\pi/2$. Thus, the diagonal anisotropies, kinetic energy and dissipation are not very different from those in the unforced decaying case.

In summary, the limiting turbulence behaviour in homogeneous shear flow in a rotating reference frame is dictated by the Taylor–Proudman theorem and is characterized by two-dimensional fluctuations. In the periodic shear case, the limiting behaviour is characterized by statistically isotropic fluctuations and turbulence decays as in unforced case.

6. DNS vs. RDT and RANS models

In this section, we compare the performances of RDT and second momentum closure models against DNS results.

6.1. *Results of RDT*

Rapid distortion theory is a well-developed linear analysis tool for investigating the Navier–Stokes equations (Pope 2000). We perform RDT analysis of the periodic shear flow using the code of Girimaji, Jeong & Poroseva (2003). In the RDT limit, the nonlinear terms are smaller compared with the linear shear term and are neglected. The effect of three different forcing frequencies ($\omega/S_{max} = 0.25, 0.5$ and 1.0) on turbulence evolution is studied. We find that the kinetic energy evolution is periodic in all cases as shown in figure 26, with minima at the initial value. The amplitude of kinetic energy variation decreases with increasing frequency. All Reynolds stress anisotropies also exhibit periodic behaviour, as can be seen from figure 27. Most notably, turbulence producing shear anisotropy (b_{12}) is periodic, with maxima at zero. Turbulence production (P) exhibits periodic behaviour about zero (figure 28) in all cases. Negative values of production are encountered just as much as positive values. Thus, the net production over any single period is zero, consistent with the behaviour of b_{12} and k. Most importantly, turbulence evolution is qualitatively the same for all forcing frequencies: it is purely periodic. Thus, RDT does not capture the different turbulence responses for different forcing frequencies.

It is somewhat surprising that the inviscid RDT results fail to capture, even qualitatively, the important features of the DNS results. On the other hand, in homogeneous
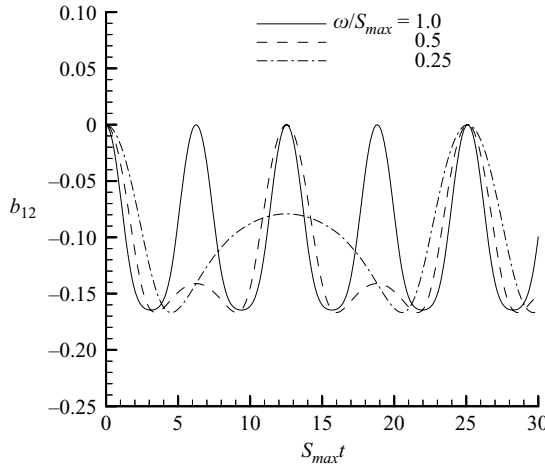
FIGURE 27. RDT evolution of b_{12} for $\omega/S_{max} = 0.25$, 0.5 and 1.0.
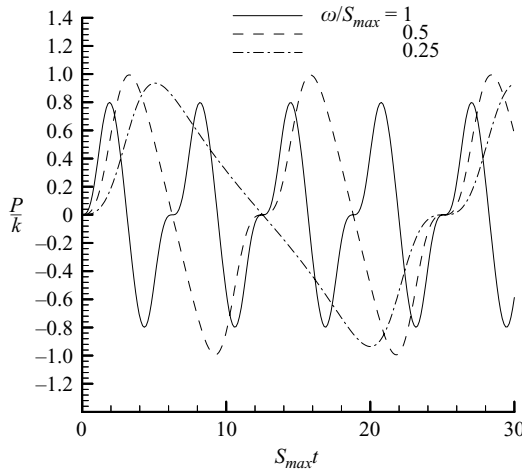

FIGURE 28. RDT production of k for $\omega/S_{max} = 0.25$, 0.5 and 1.0.

shear flow in a rotating reference frame, inviscid RDT replicates all of the main features of turbulence physics quite well. The inclusion of viscous effects alone (viscous RDT) cannot be expected to result in better agreement with DNS in the present case. Viscosity, in the rapid distortion limit, simply causes an exponential decay of the amplitude of fluctuation of each wavenumber. The decay exponent is proportional to the square of the magnitude of the wavenumber and the value of viscosity. The viscous term cannot cause an increase in the amplitude of fluctuation of any wavenumber. Thus, viscous RDT cannot possibly capture the turbulence growth observed at the low forcing frequencies. The cause for RDT failure must lie elsewhere.

We propose that the primary reason for the disparity between RDT and DNS is the time-reversibility of the mean-velocity gradient. It is well known that all inviscid turbulence process are fully time-reversible (Pope 2000): the inertial and pressure terms in the Navier–Stokes equations are invariant to a change in sign of time and total velocity. The RDT equations (equation (3.30)) have further time-reversibility

properties. Consider the following transformation:

$$t^* = -t; \quad \frac{\partial U_i^*}{\partial x_j}(t) = -\frac{\partial U_i}{\partial x_j}(t). \tag{6.1}$$

The RDT equations for the fluctuating field in terms of the transformed quantities can be written as

$$\frac{\mathrm{d}\hat{u}_j}{\mathrm{d}t^*} = -\hat{u}_k \frac{\partial U_l^*}{\partial x_k}(t) \left(\delta_{jl} - 2\frac{\kappa_j \kappa_l}{\kappa^2} \right). \tag{6.2}$$

Similarly, the wavenumber evolution equation is

$$\frac{\mathrm{d}\kappa_l}{\mathrm{d}t^*} = -\kappa_j \frac{\partial U_j^*}{\partial x_l}(t). \tag{6.3}$$

Thus, the RDT equations are invariant to changing the sign of time and mean velocity simultaneously. As a result, reversing the sign of the mean velocity gradient has the effect of reversing time. The Navier–Stokes equations are not invariant to the transformation given in (6.1) owing to the presence of terms nonlinear in the fluctuations.

Consider one cycle of sinusoidal variation of shear with time period T_0, in the interval, it is easy to see that

$$\frac{\partial U_i}{\partial x_j}\left(\frac{T_0}{2} + t \right) = -\frac{\partial U_i}{\partial x_j}\left(\frac{T_0}{2} - t \right) \quad \text{for} \quad t \leqslant \frac{T_0}{2}. \tag{6.4}$$

This feature of the mean velocity along with the time reversibility of RDT equations leads to the following:

$$u_i\left(\frac{T_0}{2} + t \right) - u_i\left(\frac{T_0}{2} - t \right) = \int_{T_0/2-t}^{T_0/2+t} \frac{\mathrm{d}u_i}{\mathrm{d}t} \, \mathrm{d}t$$

$$= \int_{T_0/2-t}^{T_0/2} \frac{\mathrm{d}u_i}{\mathrm{d}t} \, \mathrm{d}t + \int_{T_0/2}^{T_0/2+t} \frac{\mathrm{d}u_i}{\mathrm{d}t} \, \mathrm{d}t = 0. \tag{6.5}$$

The two terms in the right-hand side of the last equality are equal in magnitude, but opposite in sign. Thus, because of the reversibility property of the governing equations, the fluctuations that build up during the positive part of the shear cycle exactly unravel during the negative part of the shear cycle. At the end of each complete shear cycle, the turbulence velocity field must inevitably return to the initial condition. Thus, the RDT field is periodic. In the DNS, the presence of the nonlinear terms breaks the invariance leading to a different behaviour. A secondary reason for the disagreement between DNS and RDT is that in (temporal) proximity of zero shear, the Navier–Stokes equation cannot be linearized about the mean shear field.

In contrast to RDT, the second-moment closure RANS equations include closure models for the nonlinear and viscous effects. As the nonlinear effects are of crucial importance in this flow, the RANS model may be expected to perform better than RDT.

6.2. *RANS model predictions*

We now compare the DNS results against the predictions of Reynolds-averaged Navier–Stokes (RANS) models. Much of the observed behaviour in periodic shear turbulence can be attributed to the phase difference between the applied shear and Reynolds stress. Therefore, any one- or two-equation turbulence models that invoke the Boussinesq assumption will be invalid for periodic shear turbulence. Further,
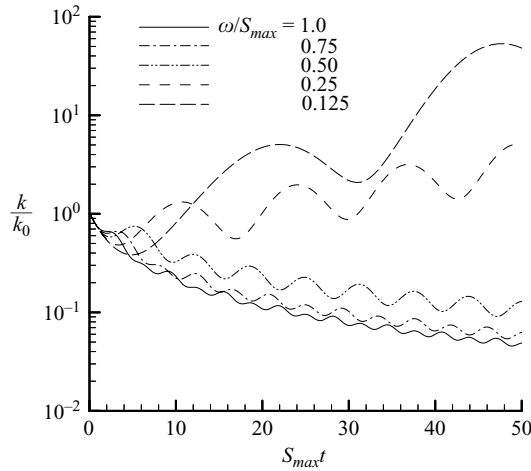
FIGURE 29. Evolution of k obtained from RANS with the LRR model for different frequencies.
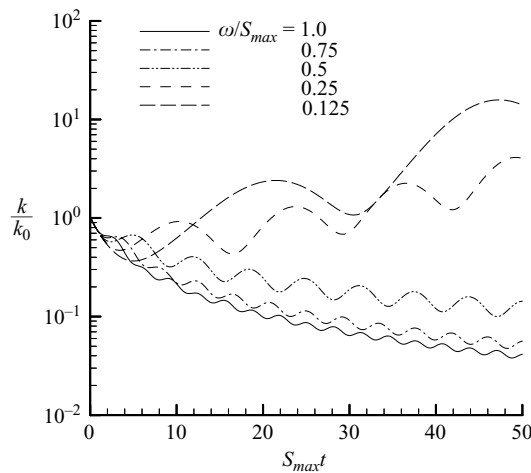

FIGURE 30. Evolution of k obtained from RANS with the SSG model for different frequencies.

any nonlinear constitutive relationship that represents stress as a function of current strain will also be invalid. The so-called structural equilibrium limit, at which the differential Reynolds-stress model can be simplified to an algebraic Reynolds-stress closure, is not achieved in this flow. Thus, the seven-equation differential Reynolds-stress closure is the lowest level at which this flow can be reasonably modeled. We investigate two differential Reynolds-stress closure models in this study: the LRR model from Launder, Reece & Rodi (1975); and the SSG model from Speziale, Sarkar & Gatski (1991).

In model simulations, the initial values of k and ε are assigned to match the initial values in the DNS. The flow is initially isotropic. The magnitude and frequency of S are the same as those in the DNS.

Figures 29 and 30 show the evolutions of k obtained from LRR and SSG models for $\omega/S_{max} = 0.125$, 0.25, 0.50, 0.75 and 1.0. Since the phase lag ϕ between stress and
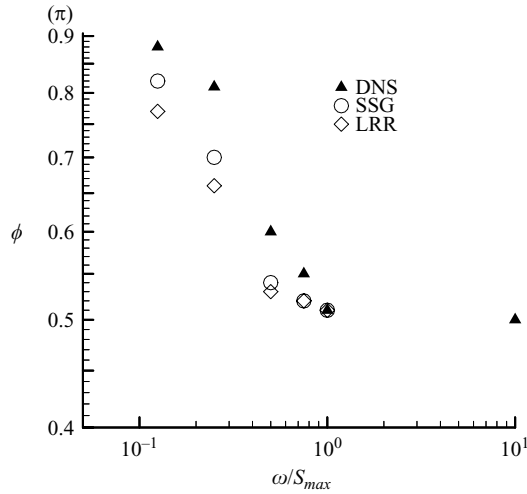
FIGURE 31. Comparison of phase lag ϕ obtained from DNS and RANS with the SSG and LRR models.

shear is crucial in predicting the net production of turbulence, the ϕ computed by the models are compared with DNS results in figure 31. Both RANS models predict turbulence growth for $\omega/S_{max} = 0.125$ and 0.25 and decay for all other frequencies. Most notably, the models predict that turbulence decays for $\omega/S_{max} = 0.5$, in contrast to the DNS result of slow growth. For the low-frequency cases, the SSG model is slightly better than LRR in predicting the evolution of k. The latter predicts a more rapid growth of k than seen in DNS results. For high-frequency cases, both models are equally inaccurate. The stress–strain phase-lags predicted by models are consistently lower (figure 31) than those by DNS. This explains why the models predict lower critical frequency value than DNS.

Next, we present the results of the diagonal anisotropy tensor obtained from the models in figure 32 for $\omega/S_{max} = 0.5$ and 1.0 cases. These predictions must be compared with DNS results in figures 17 and 19. Models predict periodic variation of normal anisotropy. The frequency of normal anisotropy is twice that of applied mean shear. For $\omega/S_{max} = 0.5$, b_{11} predicted by SSG agrees quite well with DNS, but the magnitude of b_{22} is lower than that of DNS. The LRR model predicts much smaller magnitudes for both b_{11} and b_{22}. For $\omega/S_{max} = 1.0$, both models overpredict the magnitudes of b_{11} and b_{22}. The SSG model has a relatively larger error than the LRR model. In the decay case, the normal anisotropy cycle-mean does not appear to vanish, in contrast to the behaviour in DNS.

In summary, both models predict lower values of critical frequency than that obtained by DNS. The SSG model behaves better at low forcing frequency in predicting k and normal anisotropy, while LRR is better at high frequency in predicting normal anisotropy.

6.3. Modelling implications

In the case of homogeneous shear flow in rotating reference frame, linear analysis captures much of the turbulence physics, as indicated earlier. Thus, the linear processes dominate the flows physics. The RANS modelling implication of this observation is simple. Accurate modelling of the rapid pressure–strain redistribution which is the only unclosed linear term is crucial to capturing shear flow physics in rotating
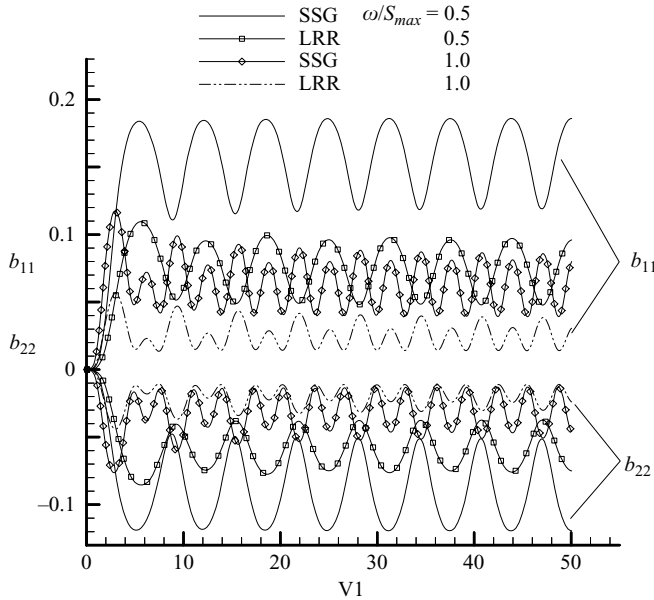
FIGURE 32. RANS predictions of b_{11} and b_{22} at two frequencies. Results to be compared with DNS data in figures 17 and 19.

reference frames. Indeed, the linear analysis can provide guidance for developing the closure model.

In the case of periodically sheared turbulence considered here, RDT does not capture the essential flow physics. The asymptotic behaviour in this case is dictated by the nonlinear processes. Thus, the onus falls on the slow pressure–strain distribution and dissipation closure models to capture the observed behaviour. In the RANS comparisons above, the rapid pressure–strain closure represents the biggest difference between the LRR and SSG models. The closures for nonlinear terms are similar. It is for this reason that both models predict qualitatively similar behaviour.

In general, the closure techniques for the rapid pressure–strain redistribution term are more sophisticated as they draw heavily from RDT (for function) and representation theory (for form). The nonlinear process closures are less formally derived and based primarily on return-to-isotropy and other empirical arguments. The present flow poses substantial challenges for closure modelling of nonlinear processes.

7. Conclusions

To understand the effects of unsteady forcing on turbulence, we perform DNS of homogeneous periodic-shear flows. Lattice Boltzmann equations are solved in a computational domain which is bounded by frictionless walls in the y-direction and is periodic in the x- and z-directions. Body force is applied to generate the desired periodic shear:

$$S = S_{max} \sin(\omega t).$$

The main findings are as follows.

(*a*) At low forcing frequencies, kinetic energy grows. At high frequencies, k decays. The critical frequency at which the asymptotic behaviour changes from growth to

decay is found to be around $\omega/S_{max} = 0.5$. At very high frequency ($\omega/S_{max} = 10$), the periodically forced turbulence behaves similarly to decaying isotropic turbulence.

(*b*) The observed behaviour can be explained in terms of the stress–strain phase-lag ϕ at different forcing frequencies. The phase-lag goes from π at low frequencies to $\pi/2$ at high frequencies. Phase-lag of $\pi/2$ corresponds to no net production. Thus, the production decreases progressively as forcing frequency increases. When the level of production falls below dissipation, turbulence cannot be sustained.

(*c*) Normal anisotropy oscillates about non-zero asymptotic values in growth cases. In decay cases, the cycle-average of anisotropy appears to vanish at long time.

(*d*) RDT does not capture the frequency-dependence of the asymptotic behaviour. It predicts periodic k-behaviour at all forcing frequencies.

(*e*) Second moment closures do capture the asymptotic frequency dependence, although the predicted critical value is smaller than that observed in DNS.

(*f*) Comparison of RDT and DNS results appears to indicate that the onus is on the closure models of the nonlinear terms to produce the observed asymptotic frequency dependence.

REFERENCES

BHATNAGAR, P. L., GROSS, E. P. & KROOK, M. 1954 A model for collision processes in gases. I. Small amplitude processes in charged and neutral one-component system. *Phys. Rev.* A **94**, 511–525.

CAMBON, C. & SCOTT, J. F. 1999 Linear and nonlinear models of anisotropic turbulence. *Annu. Rev. Fluid Mech.* **31**, 1–53.

CHAMPAGNE, F. H., HARRIS, V. G. & CORRSIN, S. 1970 Experiments on nearly homogeneous turbulent shear flow. *J. Fluid Mech.* **41**, 81–139.

CHEN, H., CHEN, S. & MATTHAEUS, W. H. 1992 Recovery of the Navier–Stokes equations using a lattice-gas Boltzmann method. *Phys. Rev.* A **45**, R5339–R5342.

DE SOUZA, F. A., NGUYEN, V. D. & TAVOULARIS, S. 1995 The Structure of highly shear turbulence. *J. Fluid Mech.* **303**, 155–167.

GIRIMAJI, S. S. 2000 Pressure–strain correlation modelling of complex turbulent flows. *J. Fluid Mech.* **422**, 91–123.

GIRIMAJI, S. S., JEONG, E. & POROSEVA, S. V. 2003 Pressure–strain correlation in homogeneous anisotropic turbulence subject to rapid strain-dominated distortion. *Phys. Fluids* **15**, 3209–3222.

GIRIMAJI, S. S., O'NEIL, J. R. & YU, O. 2006 Rapid distortion analysis of homogeneous turbulence subjected to rotating shear. *Phys. Fluids* (in press).

GUO, Z., ZHENG, C. & SHI, B. 2002 Discrete lattice effects on the forcing term in the lattice Boltzmann method. *Phys. Rev.* E **65**, 046308.

HADZIC, I., HANJALIC, K. & LAURENCE, D. 2001 Modelling the response of turbulence subjected to cyclic irrotational strain. *Phys. Fluids* **13**, 1739–1747.

HE, X. & LUO, L.-S. 1997 Theory of the lattice Boltzmann equation: from Boltzmann equation to lattice Boltzmann equation. *Phys. Rev.* E **56**, 6811–6817.

HIGUERA, F. J. & JEMENEZ, J. 1989 Boltzmann approach to lattice gas simulations. *Europhys. Lett.* **9**, 663–668.

D'HUMIÈRES, D. 1992 Generalized lattice Boltzmann equations. In *Rarefied Gas Dynamics: Theory and Simulations* (ed. D. Shizgal & D. P. Weaver) *Prog. Astro. Aero.* **159**, 450–458.

D'HUMIÈRES, D., GINZBURG, I., KRAFCZYK, M., LALLEMAND, P. & LUO, L.-S. 2002 Multiple-relaxation-time lattice Boltzmann models in three dimensions. *Phil. Trans. R. Soc. Lond.* **360**, 437–451.

JACOBITZ, F. G., SARKAR, S. & VAN ATTA, C. W. 1997 Direct numerical simulations of turbulence evolution in a uniformly sheared and stably stratified flow. *J. Fluid Mech.* **342**, 231–261.

KIDA, S. & TANAKA, M. 1994 Dynamics of vortical structures in homogeneous shear flow. *J. Fluid Mech.* **274**, 43–68.

KOELMAN, J. M. V. A. 1991 A simple lattice Boltzmann scheme for Navier–Stokes fluid flow. *Europhys. Lett.* **15**, 603–607.

LAUNDER, B. E., REECE, G. J. & RODI, W. 1975 Progress in the development of a Reynolds-stress turbulence closure. *J. Fluid Mech.* **68**, 537–566.

LEE, M. J., KIM, J. & MOIN, P. 1990 Structure of turbulence at high shear rate. *J. Fluid Mech.* **216**, 561–583.

MCNAMARA, G. & ZANETTI, G. 1988 Use of the Boltzmann equation to simulate lattice-gas automata. *Phys. Rev. Lett.* **61**, 2332–2335.

MEI, R., SHYY, W., YU, D. & LUO, L.-S. 2000 Lattice Boltzmann method for three-dimensional flows with curved boundary. *J. Comput. Phys.* **161**, 680–699.

MOIN, P. & MAHESH, K. 1998 Direct numerical simulation: a tool in turbulence research. *Annu. Rev. Fluid Mech.* **30**, 539–578.

POPE, S. B. 2000 *Turbulent Flows.* Cambridge University Press.

QIAN, Y. H., D'HUMIÈRES, D. & LALLEMAND, P. 1992 Lattice BGK models for Navier–Stokes equation. *Europhys. Lett.* **17**, 479–484.

QUADRID, M. & SIBILLA, S. 2000 Numerical simulation of turbulent flow in a pipe oscillating around its axis. *J. Fluid Mech.* **424**, 217–241.

ROGALLO, R. S. 1981 Numerical experiments in homogeneous turbulence. *NASA TM* -81315.

ROGERS, M. M. 1986 The structure and modelling of the hydrodynamic and passive, scalar fields in homogeneous turbulent shear flow. PhD thesis, Department of Mechanical Engineering, Stanford University.

ROGERS, M. M. & MOIN, P. 1987 The structure of the vorticity field in homogeneous turbulent flows. *J. Fluid Mech.* **176**, 33–66.

ROSE, W. G. 1996 Results of an attempt to generate a homogeneous turbulent shear flow. *J. Fluid Mech.* **25**, 97–120.

SALHI, A. 2002 Similarities between rotation and stratification effects on homogeneous shear flow. *Theor. Comput. Fluid Dyn.* **15**, 339–358.

SALHI, A. & CAMBON, C. 1997 An analysis of rotating shear flow using linear theory and DNS and LES results. *J. Fluid Mech.* **347**, 171–195.

SALHI, A., CAMBON, C. & SPEZIALE, C. G. 1997 Linear stability analysis of plane quadratic flows in a rotating frame with applications to modelling. *Phys. Fluids* **9**, 2300–2309.

SCHUMACHER, J. & ECKHARDT, B. 2000 On statistically stationary homogeneous shear turbulence. *Europhys. Lett.* **52**, 627–632.

SPEZIALE, C. G., GATSKI, T. B. & GIOLLA MHUIRIS, N. M. 1990 A critical comparison of turbulence models for homogeneous shear flows in a rotating frame. *Phys. Fluids* A **2**, 1678–1684.

SPEZIALE, C. G., SARKAR, S. & GATSKI, T. B. 1991 Modelling the pressure–strain correlation of turbulence: an invariant dynamical system approach. *J. Fluid Mech.* **227**, 245–272.

SPEZIALE, C. G., ABID, R. & BLAISDELL, G. A. 1996 On the consistency of Reynolds stress turbulence closures with hydrodynamic stability theory. *Phys. Fluids* **8**, 781–788.

SUCCI, S. 2001 *The Lattice Boltzmann Equation for Fluid Dynamics and Beyond.* Oxford University Press.

TAVOULARIS, S. & CORRSIN, S. 1981a Experiments in nearly homogeneous turbulent shear flow with a uniform mean temperature gradient. Part 1. *J. Fluid Mech.* **104**, 311–349.

TAVOULARIS, S. & CORRSIN, S. 1981b Experiments in nearly homogeneous turbulent shear flow with a uniform mean temperature gradient. Part 2. The fine structure. *J. Fluid Mech.* **104**, 349–367.

TAVOULARIS, S. & KARNIK, U. 1989 Further experiments on evolution of turbulent stress and scales in uniformly sheared turbulence. *J. Fluid Mech.* **204**, 457–478.

TOWNSEND, A. A. 1976 *The Structure of Turbulent Shear Flow*, 2nd edn. Cambridge University Press.

YU, D. & GIRIMAJI, S. S. 2005 DNS of homogeneous shear turbulence revisited with the lattice Boltzmann method. *J. Turb.* **6** (6), 1–17.

YU, D. MEI, R. LUO, L.-S. & SHYY, W. 2003 Viscous flow computations with the method of lattice Boltzmann equation. *Prog. Aerospace Sci.* **39**, 329–367.

YU, H., GIRIMAJI, S. S. & LUO, L.-S. 2005a Lattice Boltzmann simulations of decaying homogeneous isotropic turbulence with and without system rotation. *Phys. Rev.* E **71**, 204501.

YU, H., GIRIMAJI, S. S. & LUO, L.-S. 2005b DNS and LES of decaying isotropic turbulence with and without frame rotation. *J. Comput. Phys.* **209**, 509–616.